ARL-TR-10136 ● JULY 2025

Shear Band Characteristics of Metals with Porosity and Viscosity

by John D. Clayton

DISTRIBUTION STATEMENT A. Approved for public release: distribution unlimited.

NOTICES

Disclaimers

The findings in this report are not to be construed as an official Department of the Army position unless so designated by other authorized documents.

Citation of manufacturer's or trade names does not constitute an official endorsement or approval of the use thereof.

Destroy this report when it is no longer needed. Do not return it to the originator.

ARL-TR-10136 ● JULY 2025

Shear Band Characteristics of Metals with Porosity and Viscosity

John D. Clayton
DEVCOM Army Research Laboratory

DISTRIBUTION STATEMENT A. Approved for public release: distribution unlimited.

REPORT DOCUMENTATION PAGE

1. REPORT DATE	2. REPORT TYPE	3. DATES COVERED	
		START DATE	END DATE
July 2025	TECHNICAL REPORT	01 Oct 2024	31 July 2025

4. TITLE AND SUBTITLE
Shear Band Characteristics of Metals with Porosity and Viscosity

5a. CONTRACT NUMBER	5b. GRANT NUMBER	5c. PROGRAM ELEMENT NUMBER
5d. PROJECT NUMBER	**5e. TASK NUMBER**	**5f. WORK UNIT NUMBER**

6. AUTHOR(S)
John D. Clayton

7. PERFORMING ORGANIZATION NAME(S) AND ADDRESS(ES)
DEVCOM Army Research Laboratory
ATTN: FCDD-RLA-TB
Aberdeen Proving Ground, MD 21005-5066

8. PERFORMING ORGANIZATION REPORT NUMBER
ARL-TR-10136

9. SPONSORING/MONITORING AGENCY NAME(S) AND ADDRESS(ES)	10. SPONSOR/MONITOR'S ACRONYM(S)	11. SPONSOR/MONITOR'S REPORT NUMBER(S)

12. DISTRIBUTION/AVAILABILITY STATEMENT
DISTRIBUTION STATEMENT A. Approved for public release: distribution unlimited.

13. SUPPLEMENTARY NOTES
ORCID: John D. Clayton, 0000-0003-4107-6282

14. ABSTRACT
Initial defects such as voids or material imperfections increase susceptibility to adiabatic shear failure in ductile metals as demonstrated in prior experimental, analytical, and numerical investigations. Viscosity in the shear band, manifesting macroscopically as strain-rate sensitivity, inhibits localization. An analytical shear band process zone model is advanced to account for porous and viscous phenomena. The material contains an average defect measure (e.g., porosity) and a concentrated defect measure at a spatial location where shear banding is most likely to initiate after an instability threshold is attained. Shearing resistance and certain physical properties are reduced commensurately with local defect concentration. Non-Newtonian viscosity increases dissipative resistance. Viscous dissipation, if strong enough, is shown to prevent an infinitesimal-width shear band even in a non-conductor. A pseudo-quadratic viscosity widens the band similarly to heat conduction, and akin to quadratic shock viscosity used in hydrocodes to resolve widths of planar shock waves. The model captures simulation data showing reduced localization strain and shear band width with increasing maximum initial pore size in additively manufactured titanium and HY-100 steel. Predictions for shear band width, local strain, and temperature are more accurate versus experimental data on steel than prior analytical modeling. A quantitative framework is established by which processing defects (e.g., as arising in additive manufacturing) and slip-band strength dependence on shearing rate can be related to shear band characteristics.

15. SUBJECT TERMS
Shear Localization, Plasticity, Porosity, Steel, Titanium, Additive Manufacturing, Terminal Effects

16. SECURITY CLASSIFICATION OF:			17. LIMITATION OF ABSTRACT	18. NUMBER OF PAGES
a. REPORT	b. ABSTRACT	C. THIS PAGE		
UNCLASSIFIED	UNCLASSIFIED	UNCLASSIFIED	UU	43

19a. NAME OF RESPONSIBLE PERSON	19b. PHONE NUMBER *(Include area code)*
John D. Clayton <john.d.clayton1.civ@army.mil>	(520) 691-5636

STANDARD FORM 298 (REV. 5/2020)
Prescribed by ANSI Std. Z39.18

Contents

List of Figures iv

List of Tables v

Preface vi

Acknowledgments vii

1. Introduction 1

2. Rigid-Plastic Analysis 6

3. Shear Band Governing Equations 9

4. Analytical Solution 12

5. Results 16

5.1 Parameterization 16

5.2 Comparison with Data 18

5.3 Effects of Viscosity and Defects 23

5.4 Discussion 27

6. Conditions at Initial Instability 29

7. Porosity Data and Defect Concentrations 31

8. Conclusions 32

9. References 34

List of Symbols, Abbreviations, and Acronyms 40

Distribution List 43

List of Figures

Figure 1. Boundary value problem for shear localization pioneered by Grady. A shear band evolves in a background material of dense flow strength τ_y, temperature θ_y, strain rate $\dot{\gamma}$, and porosity ϕ_0 newly introduced here. Shear band of width a initiates where local defect concentration is larger by $\Delta\phi$. Shear displacement in fully formed band of process zone length ζ_b is $\delta_b = 2\psi_c$; excess shear strain in band is $\gamma_b = \delta_b/a$. Interfacial distance ξ demarcating unloaded rigid domain increases with time while stress relaxes in band. At the rigid-plastic interface, $\tau_0 = \tau_y = \tau/(1-\phi_0)$. Shear band energy per unit area of dense matrix is $\Gamma = \tau_y\psi_c/2$. Momentum and heat diffuse only in the x-direction; δ_b and ζ_b are outcomes of the analysis. 7

Figure 2. Critical average shear strain γ_c vs. normalized defect concentration $A\Delta\phi/\phi_0$: (a) model with and without heat conduction for Ti at $\dot{\gamma} = 10^3$/s vs. numerical simulation data (b) model for HY-100 steel at $\dot{\gamma} = 10^3$/s vs. data (c) model for Ti at $\dot{\gamma} = 10^3$/s and $\dot{\gamma} = 10^4$/s (d) model for HY-100 steel at $\dot{\gamma} = 10^3$/s and $\dot{\gamma} = 10^4$/s. When heat conduction is omitted, default viscosity is found from Equation 37. Fitted viscosity in (b) is tuned to 1.13 times default from Equation 37 to match result with conduction enabled. 19

Figure 3. Predicted influence of defect (excess pore) concentration $A\Delta\phi/\phi_0$ on shear band characteristics of Ti and HY-100 steel; properties of Table 1: (a) $\gamma_c - \gamma_p$ (b) γ_b (c) a (d) δ_b (e) ζ_b (f) t_c (g) θ_c (h) Γ. 21

Figure 4. Influence of viscosity η on shear band characteristics, two defect concentrations $\Delta\phi/\phi_0$, $\eta_0 = 6.5 \times 10^{-4}\mathrm{kg/m}$, properties for HY-100 steel of Table 1: (a) γ_c (b) γ_b (c) a (d) δ_b (e) ζ_b (f) t_c (g) θ_c (h) Γ. 25

Figure 5. Influence of degradation factor ω on shear band characteristics, two defect concentrations $\Delta\phi/\phi_0$, $\omega_0 = 0.025$, other properties for HY-100 steel of Table 1: (a) γ_c (b) γ_b (c) a (d) δ_b (e) ζ_b (f) t_c (g) θ_c (h) Γ. 26

List of Tables

Table 1. Properties or parameters used in calculations for Ti and HY-100 steel. 18

Table 2. Results comparison for HY-100 steel, $\dot{\gamma} = 1350/\mathrm{s}$. 22

Table 3. Shear band width comparison for HY-100 steel, $\dot{\gamma} = 1350/\mathrm{s}$, $L = 2h = 2.5\,\mathrm{mm}$. 23

Table 4. Porosity and critical strain γ_c at $\dot{\gamma} = 10^3/\mathrm{s}$: realizations R1, . . . , R10 of Vishnu et al. 32

Preface

This report encompasses and extends a recent theoretical analysis published by the author in the *Journal of Applied Mechanics*.[1] The present report includes detailed steps in theoretical derivations excluded from the original article primarily due to journal page limitations. This report also contains additional calculated results and discussion likewise excluded from the original article for brevity. A list of notation is newly included in this report to facilitate understanding and transition of derived formulae to future applications.

[1] Clayton JD. Analytical shear-band process zone model incorporating nonlinear viscous effects and initial defects. Journal of Applied Mechanics. 2025; 92: 091009.

Acknowledgments

I would like to thank Dr. Chris Meredith for technically reviewing this report and the original journal article. I would also like to acknowledge the support of ARL's Terminal Effects competency.

1. Introduction

The present work, like the original article[1] from which this extends, derives and implements an analytical model for shear band characteristics—namely, terminal shear band width, internal shear strain, surface energy, temperature, and for torsional loading, the critical applied strain. Novel features are consideration of material porosity and non-Newtonian viscosity for the singular surface used in the analysis to describe microscopic physics of the band.

Adiabatic shear localization is an important phenomenon in metals deformed at high rates, whereby heat conduction is limited by short time scales. At some threshold strain, softening by thermal, geometric, and/or structural transformation mechanisms overtakes strain- and strain-rate hardening, leading to instability. Localization into one or more thin bands of rapidly deforming material of large strain and high temperature relative to surrounding material occurs at some time after the instability threshold. Shear stress drops commensurately as the material unloads, and ductile fracture often, but not always, occurs in later stages of the process. See the seminal book by Wright[2] and a more recent review article by Yan et al.[3] for background.

In a torsion experiment, the macroscopic strain when this rapid stress drop initiates is typically termed the "critical strain" (e.g., Molinari and Clifton[4]). Strain-rate sensitivity tends to reduce shear band susceptibility. Thermal diffusivity increases critical strain, especially at low applied strain rates,[2] and provides a regularization length lending the shear band a finite width or thickness. Inertia increases critical strain at high applied strain rates,[5] with momentum diffusion thought to prevent the shear band from attaining an infinite width.[6]

While certain physics, including (an approximate lower bound on) critical strain, can be modeled under adiabatic and quasi-static approximations,[2,4,7,8] a shear band's width and internal strain cannot be predicted under such approximations in the general case. In the absence of an intrinsic length scale supplied by the constitutive model (e.g., conduction or a regularized damage-fracture model[9,10]), the width of the band is dictated by boundary conditions and any initial perturbations in geometry or material properties. Although strain-rate sensitivity can provide an implicit length scale instilling unique (numerical) solutions,[11] the band size is controlled by the geometry and initial conditions in the absence of intrinsic regularization. Since heat conduction is paramount with regard to shear band width in typical metals, with

none being perfect insulators, labeling such localization bands as “adiabatic” is an obvious misnomer.[2,12]

In the oft-analyzed setting of simple shear of a thermoviscoplastic solid with uniform, thermally insulated far-field boundary conditions,[2,4,13,14] the homogeneous solution is the unique solution, and localization does not occur. A local perturbation such as a geometric defect, strength heterogeneity, or temperature spike is needed to physically induce a spatially nonhomogeneous solution to the governing equations. Localized solutions can also be instilled, nonphysically, in broader computer simulations of dynamic deformation of this class of materials by minute numerical perturbations—e.g., floating-point error. Depending on the loading conditions, regions of high shear strain initiate at multiple locations if defect distributions exist.[15–18] However, in typical dynamic experiments on thin-walled tubes in a torsional split-Hopkinson (pressure) bar (i.e., SHPB or Kolsky bar),[19–22] and some numerical simulations of the process,[17] failure is usually dictated by behavior of one dominant shear band that grows most rapidly. In this setting, growth of narrowly spaced, nascent bands is arrested by stress release from the dominant band(s).[23]

Additive manufacturing (AM) with metallic materials often produces structures with nonnegligible porosity or void space.[24–26] As might be expected, pores act as preferential sites for localized deformation, including shear banding. Mechanisms include enhanced local deformation leading to thermal softening, inter-void linking, and ductile fracture.[27–29] In SHPB torsion, porous material tends to show a reduced critical strain for localization relative to fully dense material, as evidenced by experiment[30] and simulation.[17] In the latter, dominant shear bands tended to nucleate where void diameters and local void volume fractions were largest. Although increasing the average porosity also reduced critical strain, local void concentration had a greater effect; furthermore, larger pores are naturally more probable as the average porosity increases. Similar trends were observed in ring-compression simulations.[18] In such simulations,[17,18] as well as prior analytical studies,[2,4,7,8,31] localization was impeded by viscoplastic effects manifested through strain-rate sensitivity.

The objective of the present study is derivation and implementation of an analytical framework for physical characteristics of shear bands in viscous metals with initial defects (e.g., porosity from AM). Closed-form expressions for critical strain or

localization time are sought, along with expressions for the width of the band and its average internal strain and temperature, all of which can be compared with experimental data (e.g., Giovanola[32] and Duffy and Chi[20]). While contemporary numerical simulations allow for closer representation of complex constitutive behaviors[33–36] and microstructures,[37] these are time-intensive, require software expertise, and must generally be repeated for each new material system. Relatively simple analytical expressions, if accurate, facilitate an immediate physical understanding and suggest design guidelines. For example, if the most important material properties and parameters can be identified in an analytical framework, then particular materials and microstructures can be targeted or optimized for a given application. In the present context, one may seek a material to minimize or maximize the critical localization strain for a given applied strain rate and constraints on average flow stress, mass density, etc. In particular, for porous metals as produced by AM, a mathematical framework is sought by which effects of local defect concentration affect adiabatic shear. Of course, some physical rigor must be sacrificed to produce a tractable problem yielding expressions simple enough to be evaluated without numerical iteration.

The 1-D simple shear problem is analyzed herein. As reviewed elsewhere,[2,3] this problem has been the subject of many prior analytical studies, though none appear to address effects of heterogeneous porosity in the manner postulated here. The goal is *not* to develop a new (3-D) constitutive model for porous ductile metals as in representative prior works,[28,29,38] but rather to describe the 1-D shear band problem using basic constitutive assumptions specialized to simple shear. Several well-known analytical expressions for shear band width made assumptions on steadiness of the late-stage flow process in the band.[12,39,40] The steady flow assumption has been questioned by finite-difference computations,[14] and while these analytical expressions all include thermal diffusivity, and those of several authors[12,40] include rate sensitivity, they all omit momentum diffusion.

In contrast, the analytical shear band process zone model of Grady, most thoroughly derived in a 1992 article,[6] accounts for dynamic stress release as well as heat conduction. The standard form of the model[41,42] omits rate dependence, but a linear viscous stress (i.e., Newtonian viscosity) was investigated briefly by Grady.[6] Origins of the model stem from seminal work of Mott[43]—namely, an analytical solution for tensile expansion and release of a fragmenting cylindrical ring, later enhanced by

Kipp and Grady.[44] Grady and Kipp applied such concepts to predict spacing of shear bands witnessed in shock-wave compression.[23,45] This led to more formal treatments of the shear band evolution process and shear band toughness by Grady.[6,41,42]

A recent theoretical study[46] extended the rate-independent models of Grady and Kipp to include an intermediate viscoplastic unloading zone and rate-dependent response of the far-field plastic material. By including these extra features, closer agreement with certain data was reported;[46] for example, the original model[6] tended to predict narrower bands of higher strain than witnessed experimentally,[32] whereas viscoplasticity widens the band and reduces its maximum strain. However, additions by Sheng et al.[46] complicate the analysis and final expressions, and values to be used for some of the constants and factors in the solution are unclear or are not reported. As discussed later, the model by Sheng et al.[46] would also seem to severely overestimate temperature rise in the band.

In the current work, Grady's theory[6] is newly augmented with a non-Newtonian viscosity for the shear slip zone to account for rate dependence and provide a more diffuse shear band as seen experimentally. The particular form of viscosity is quadratic, but the viscosity coefficient is normalized by the ambient background strain rate such that a linear form is recovered when the shear band's internal strain rate matches that of the background. The value of the viscosity coefficient for slip discontinuity correlates loosely with strain-rate sensitivity of the continuum. Noting that strain-rate sensitivity exponents are much smaller than unity, the model does *not* surmise a linear or quadratic viscosity for the background continuum, but only for the local slip discontinuity. The proposed increasing viscous stress with increasing slip velocity could be justified, conceptually, by the increase in strain-rate sensitivity with rate witnessed in experiments on similar metals to those studied here.[8,47,48]

The derived solution for shear band characteristics contains a dependence on viscosity coefficient that is nearly identical to dependence on thermal diffusivity. Unlike the linear viscosity introduced briefly by Grady,[6] the nonlinear viscosity enables a finite shear band width even in the absence of conduction, and it further allows for convenient closed-form expressions precluded by a linear viscosity or a viscoplastic continuum.[46] The quadratic viscosity is similar to the quadratic shock viscosity used to lend a finite width to shock waves when viscous dissipation is otherwise absent.[49,50] Although often termed "artificial," such shock viscosity can be justified to represent

real physical behavior (e.g., in gas dynamics[50]). Analogously, the viscosity assigned herein can be used to represent the true observed width of a shear band, even in cases where the underlying material is fully adiabatic as in numerical simulations.[17,18] Non-Newtonian viscosity thereby lends regularization from dissipative microscopic processes not captured by heat conduction.

A second new component of the proposed model accounts for initial defect concentrations. A dominant shear band is assumed to initiate at the instability threshold,[2,5,51] or at some finite time thereafter, at the spatial location where defect density is highest relative to the average defect content (e.g., average porosity) of the background material, as corroborated by numerical studies.[17,18,28] Weakening of material in the slip band is accelerated by the defect concentration, manifesting by a linear damage-type model whose single parameter controls the rate of degradation. For a porous material, degradation manifests from increased geometric softening and possible void linkage and fracture. Viscous forces and thermal diffusivity are also reduced by defects. The model preserves simple closed-form expressions for band characteristics derived by Grady,[6] with unavoidable complexity encompassed by relationships between a damage constitutive parameter and microstructure or geometry.

Herein, both the viscous and defect-related parameters are quantified using numerical data from simulations of dynamic torsion SHPB tests on titanium (Ti) and steel with discrete voids.[17] Although the data present significant scatter, the model correctly captures the trend of reduced critical strain, and a narrower band, with increasing local defect concentration. A thinner band of lower final temperature is predicted as defect concentration increases, implying a more brittle response with increasing local porosity. A very recent generalization[52] of Grady's model allows strength degradation from microstructure processes such as dynamic recrystallization (DRX; Rittel et al.[53]); effects of thermal- and microstructure-softening on dissipated energy are quantified via temperature measurements.

Sections 2, 3, and 4 report the transient boundary value problem, governing equations, and their solution. Results follow in Section 5, including comparison with numerical and experimental data. Section 6 discusses instability criteria used to specify initial conditions at nucleation, and Section 7 explains defect concentration measures. A thorough list of notation follows the conclusions of Section 8 and bibliography of Section 9.

2. Rigid-Plastic Analysis

The problem setup is similar to that of Grady,[6,41] two major exceptions being (i) the solid may contain pores or other defects, and (ii) rate sensitivity is included. The material, presumably a ductile polycrystalline metal, is isotropic, incompressible, and rigid-viscoplastic (i.e., negligible elastic shear strain[2,4,8]). A planar shear band forms in an effectively infinite, 2-D medium, as shown in Figure 1. Spatial coordinates are (x, y), with $|x|$ denoting distance from the center of the band.

The band can either nucleate homogeneously across the entire y-domain or nucleate at a specific point, say y_0, and then propagate in the $+y$-direction. Thickness a of the band is assumed constant,[6,41] but the mean shear strain $\gamma_b = \delta_b/a$ in the band increases from the start time for nucleation, labeled as the datum $t = t_0$, to a critical time t_c when the band ceases to evolve.[6,46] At $t = t_c$, stress supported by the band goes to zero, and either the material melts or fractures immediately thereafter, or the experimental apparatus assumed to instantly unload without further applied strain. Detailed modeling of the dynamics of these terminal post-failure and elastic unloading processes, for $t > t_c$, are beyond the current scope. Phase transitions[8,10,54] are excluded.

If the band is propagating, the length of the process zone wherein γ_b steadily increases is ζ_b. Behavior of the band itself is collapsed to that of a singular surface at $x = 0$.[6,23,41,45] The magnitude of shear slip supported by the upper and lower halves of the band is $\psi(t)$. In the fully formed band, the shear slip displacement parallel to the y-coordinate axis is $\psi(t_c) = \psi_c = \delta_b/2$ for $x > 0$ and $\psi_c = -\delta_b/2$ for $x < 0$, with a jump of δ_b as in Figure 1. Material is either in a state of simple shear, a rigid-body state, or at a singular boundary demarcating such states. With increasing t, stress supported by the band decreases, and a relaxation wave propagates symmetrically in $\pm x$ directions. From symmetry, analysis can be limited to domain $x \geq 0$. Assuming $\zeta_b \gg \delta_b \gg a$, verified a posteriori, y dependence is temporarily ignored and the problem is analyzed in (x, t) space.[6,41]

Material far away from the band is in a state of simple shear at constant strain rate $\dot{\gamma} > 0$, temperature θ_y, porosity ϕ_0, and Cauchy shear stress τ_y per unit area of dense matrix. All of these likely evolve during shear band evolution, but the far-field state is assumed stationary[6,41,46] to render the analysis tractable; the local state in the band is assumed to change much more drastically than that far outside.

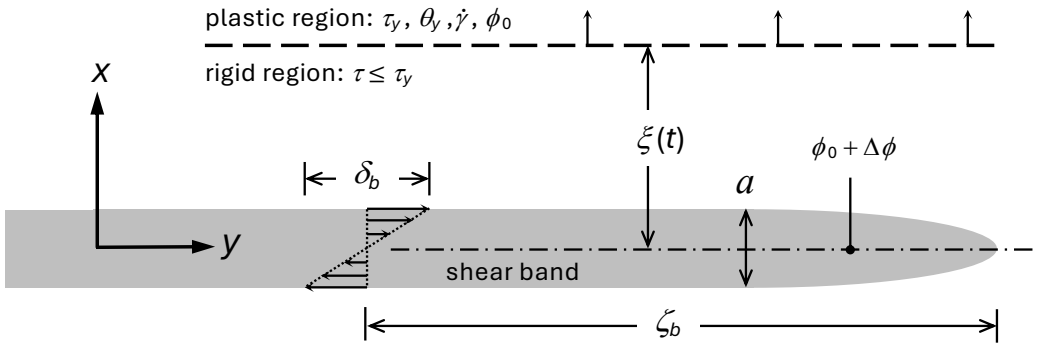

Figure 1. Boundary value problem for shear localization pioneered by Grady.[6,41] A shear band evolves in a background material of dense flow strength τ_y, temperature θ_y, strain rate $\dot{\gamma}$, and porosity ϕ_0 newly introduced here. Shear band of width a initiates where local defect concentration is larger by $\Delta\phi$. Shear displacement in fully formed band of process zone length ζ_b is $\delta_b = 2\psi_c$; excess shear strain in band is $\gamma_b = \delta_b/a$. Interfacial distance ξ demarcating unloaded rigid domain increases with time while stress relaxes in band. At the rigid-plastic interface, $\tau_0 = \tau_y = \tau/(1-\phi_0)$. Shear band energy per unit area of dense matrix is $\Gamma = \tau_y\psi_c/2$. Momentum and heat diffuse only in the x-direction; δ_b and ζ_b are outcomes of the analysis.

If the initial defect distribution is nonuniform, the shear band nucleates where defect concentration increases by $\Delta\phi$. Variations in $\phi(x)$ for $2|x| > a$ are ignored: material is treated as homogeneous away from the band. When the band is idealized as a singular surface, effects of $\Delta\phi$ are concentrated at $x = 0$ with $\phi = \phi_0$ for $|x| > 0$.

Away from singular surfaces, continuum laws for conservation of mass, momentum, and energy are, respectively (e.g., Clayton[55]),

$$\rho = (1-\phi_0)\rho_0, \qquad \frac{\partial \tau}{\partial x} = \rho\dot{v}, \qquad \rho c\dot{\theta} = \beta\tau\frac{\partial v}{\partial x} + k\frac{\partial^2\theta}{\partial x^2}. \tag{1}$$

Ambient mass density is ρ; density of material without voids is ρ_0. Particle velocity in the y-direction is $v(x,t)$, and τ is the xy-component of the Cauchy stress tensor. Dots denote partial time derivatives at fixed x, noting Eulerian and Lagrangian x-coordinates coincide. Because constitutive functions are assumed independent of pressure, the analysis does not allow superposed tensile stress that might instill void growth or compressive stress that might cause pore collapse. Specific heat per unit mass is $c = \text{const} > 0$, with any distinction between constant-pressure and constant-volume irrelevant due to incompressibility. The Taylor-Quinney factor $\beta > 0$ denoting instantaneous fraction of plastic work converted to heat is assumed constant as is typical,[4,46,52] though experiment, theory, and simulation support its

variability for many metals.[2,56–59]

Away from the band, stress[38,60,61] and conductivity vary constitutively with porosity:

$$k = (1-\phi_0)k_0 = \rho c \chi_0, \qquad \tau(x,t) = (1-\phi_0)\tau_0(x,t). \tag{2}$$

Stress supported by the dense matrix material in the absence of voids is τ_0, and k_0 likewise is conductivity of the dense solid. Thermal diffusivity $\chi_0 = k/(\rho c) = k_0/(\rho_0 c)$ is independent of ϕ_0. The second and third expressions in Equation 1 become

$$\partial\tau_0/\partial x = \rho_0 \dot{v}, \qquad \rho_0 c\dot{\theta} = \beta\tau_0(\partial v/\partial x) + k_0(\partial^2\theta/\partial x^2). \tag{3}$$

In the plastic region of Figure 1, $\tau_0 = \tau_y = \text{const}$, $\dot{v} = 0$, $\partial v/\partial x = \dot{\gamma} = \text{const}$, and $\theta = \theta_y = \text{const}$ during rapid evolution of the shear band. Strain hardening, thermal softening, and adiabatic temperature rise in the last of Equation 3 are omitted in the far-field region,[6,46] but only in the brief time domain $t \in (t_0, t_c]$. These physics are included for $t \le t_0$.

In the singular description of the shear plane, stress degrades linearly[6,41] with shear displacement $\psi(t)$ in an assumed form of the solution; the constitutive model for τ supported by the singular surface follows in Section 3. Along $x = 0$,

$$\tau(\psi(t)) = (1-\phi_0)\tau_0(\psi(t)) = (1-\phi_0)\tau_y(1-\psi(t)/\psi_c) \quad \Rightarrow \quad \tau_0 = \tau_y(1-\psi/\psi_c), \tag{4}$$

noting $\psi \in [0, \psi_c]$. Recalling $\dot{\gamma} = \text{const} > 0$, the velocity field in the two regions of Figure 1 obeys

$$v(x) = \begin{cases} \dot{\gamma}\xi, & x \in [0,\xi), \\ \dot{\gamma}x, & x \in [\xi,\infty). \end{cases} \tag{5}$$

Linear momentum in the y direction per unit area of the $x = 0$ plane of the entire body is P:

$$P(t) = \int_0^\infty \rho v \, \mathrm{d}x = (1-\phi_0)\rho_0\dot{\gamma}\xi^2 + (1-\phi_0)\rho_0\dot{\gamma}\int_\xi^\infty x \, \mathrm{d}x. \tag{6}$$

In the singular-surface description of the band, $\Delta\phi$ is excluded from the integral. Net force in the y direction, per unit area, supported by any finite region $\{B_0 : 0^+ \le x \le R\}$, where $R \in [\xi, \infty)$, is $F(t) = \tau_y(1-\phi_0) - \tau(t)$. A global momentum balance for B_0

is, dividing by $1-\phi_0$ and using Equation 4,

$$F = \frac{\mathrm{d}P}{\mathrm{d}t} \quad \Rightarrow \quad \tau_y - \tau_0(t) = \tau_y \frac{\psi(t)}{\psi_c} = \rho_0 \dot{\gamma} \xi(t) \frac{\mathrm{d}\xi(t)}{\mathrm{d}t}; \qquad \frac{\mathrm{d}\psi(t)}{\mathrm{d}t} = \dot{\gamma}\xi(t). \quad (7)$$

Velocity $\mathrm{d}\psi/\mathrm{d}t$ must match that of the rigid region. The initial datum is taken as $t_0 = 0$; thus t is negative up to the start of localization. Relations in Equation 7 with $\psi(0) = \xi(0) = 0$ have the following analytical solution,[23] easily verified a posteriori:

$$\psi(t) = \frac{\tau_y \dot{\gamma}}{18\rho_0 \psi_c} t^3, \qquad \xi(t) = \frac{\tau_y}{6\rho_0 \psi_c} t^2; \qquad \psi_c^2 = \frac{\tau_y \dot{\gamma}}{18\rho_0} t_c^3. \quad (8)$$

Note $\psi_c = \psi(t_c)$ is an outcome of the analysis, not a material property or prescribed parameter. Applying similar arguments to a truncated region $\{B_x : x_0 \le x \le R\}$ provides the linear increase versus distance for matrix stress $\tau_x = \tau(x_0)/(1-\phi_0)$ at any $x_0 \in (0, \xi)$ and t implied in the analogous treatment of Grady[6] that excludes porosity: $\tau_y - \tau_x = (1 - x_0/\xi)(\tau_y - \tau_0)$.

3. Shear Band Governing Equations

A constitutive equation distinct from Equation 4 relates local shear stress, τ, on the plane of the shear band to the slipped distance ψ, local temperature θ, and rate of slip $\dot{\psi} = \mathrm{d}\psi/\mathrm{d}t$. This equation is independent from Equation 4. A local energy balance relates temperature rise to dissipation on the slip surface and heat transfer between the band and its environment. Though motivated from continuum theory, these are discrete, rather than continuum, governing equations, specialized to the discrete surface $x = 0$.

The constitutive law for shear stress is defined as follows. Extending the equation of Grady[6] to allow for degradation from local defects and stiffening from nonlinear viscosity,

$$\begin{aligned} \tau(\psi, \dot{\psi}, \theta) &= (1-\phi_0)\tau_0(\psi, \dot{\psi}, \theta) \\ &= (1-\phi_0)(1 - \alpha\Delta\theta - \Lambda\psi/\psi_c)\tau_y + (1-\phi_0)(\dot{\psi}/a)^2\eta_e. \end{aligned} \quad (9)$$

Linear thermal softening parameter $\alpha > 0$ is defined in terms of melt temperature and other physical properties later. Local temperature excursion is $\Delta\theta = \theta - \theta_y$. The factor $\Lambda \in [0, 1)$ is a function of ϕ_0 and concentration $\Delta\phi$. The larger the value of Λ, the more rapid the loss of strength in the band due to geometric or damage-softening

from these concentrated defects. As $\Lambda \to 1$, the material becomes more brittle. A complementary degradation factor $\lambda = 1 - \Lambda$ is of the form

$$\lambda = \lambda(\Delta\phi, \phi_0) = 1 - \Lambda(\Delta\phi, \phi_0), \quad \lambda(0, \phi_0) = 1, \quad \lambda \in (0, 1]. \tag{10}$$

Noting $2\dot{\psi}/a$ is nominal shear strain rate over width a, effective quadratic viscosity is $\eta_e/4$. This can depend on microstructure (e.g., defects), temperature, and $\dot{\gamma}$ as defined later, the relative strain rate of the background continuum. Motivation for nonlinear viscosity of the shearing interface was discussed in Section 1. Dividing Equation 9 by $1 - \phi_0$,

$$\tau_0 = \tau_y(1 - \alpha\Delta\theta - (1 - \lambda)\psi/\psi_c) + \eta_e(\dot{\psi}/a)^2; \qquad \eta_e = \eta_e(\theta, \Delta\phi, \phi_0, \dot{\gamma}). \tag{11}$$

Eliminating τ_0 using Equation 4 and substituting ψ and $\dot{\psi}$ from Equation 8, temperature rise in the shear band is

$$\begin{aligned} \theta(t) - \theta_y &= \frac{1}{\alpha}\left[\frac{\lambda}{\psi_c}\psi + \frac{\eta_e}{\tau_y a^2}\dot{\psi}^2\right] = \frac{\tau_y\dot{\gamma}}{18\alpha\rho_0\psi_c^2}\left[\lambda t^3 + \frac{\eta_e\dot{\gamma}}{2\rho_0 a^2}t^4\right] \\ &= \frac{1}{\alpha}\left(\frac{t}{t_c}\right)^3\left[\lambda + \frac{\eta_e\dot{\gamma}}{2\rho_0 a^2}t\right]. \end{aligned} \tag{12}$$

A second equation for temperature is furnished by an energy balance; a discrete analog of Equation 1 is

$$\rho c\dot{\theta} = \beta\tau\frac{2\dot{\psi}}{a} - \frac{2k_e}{a^2}\Delta\theta \quad \Rightarrow \quad \dot{\theta} = \frac{2\beta}{\rho_0 ca}\tau_0\dot{\psi} - \frac{2\chi_e}{a^2}\Delta\theta; \quad \chi_e = \chi_e(\theta, \Delta\phi, \phi_0). \tag{13}$$

Derivative $\partial^2\theta/\partial x^2 \approx -2\Delta\theta/(a^2)$ is a second-order difference[6,41,42] centered at $x = 0$ of grid spacing a and vanishing $\Delta\theta$ at $x = \pm a$. Effective diffusivity of the band surface $\chi_e = k_e/(\rho_0 c)$, enriching constant diffusivity χ_0 of the homogeneous background in Equation 3, can depend on local temperature and defects. From Equation 12, where θ_c and η_c are temperature change and viscosity at t_c,

$$\theta_c = \theta(t_c) - \theta_y = \lambda/\alpha + \eta_c\dot{\gamma}\, t_c/(2\alpha\rho_0 a^2); \qquad \eta_c = \eta_e(\theta_c, \Delta\phi, \phi_0, \dot{\gamma}). \tag{14}$$

As in prior models,[6,41,46] the energy balance in Equation 13 is weakly enforced, in integral form, over the time spanned by band evolution. Noting $\psi(t_c) = \psi_c$,

$\mathrm{d}\,\Delta\theta = \dot{\theta}\mathrm{d}t$, $\mathrm{d}\psi = \dot{\psi}\,\mathrm{d}t$ and using Equation 4,

$$\theta_c = \int_0^{\theta_c} \mathrm{d}\theta = \frac{2\beta}{\rho_0 ca}\int_0^{\psi_c} \tau_0\,\mathrm{d}\psi - \frac{2}{a^2}\int_0^{t_c} \chi_e \Delta\theta\,\mathrm{d}t = \frac{\beta\tau_y}{\rho_0 ca}\psi_c - \frac{2\lambda\chi_0}{a^2}\int_0^{t_c} \Delta\theta\,\mathrm{d}t. \tag{15}$$

The rightmost expression assumes an implicit functional form for θ dependence of χ_e: averaged over the duration of shear banding, diffusivity degrades similarly to stress by a factor of λ. Defects can induce cracks or tears in the material and an effective temperature rise in micro-bands between voids, all of which serve to decrease conductivity k_e and more so, viscosity η_e. The latter at t_c is

$$\eta_c(\Delta\phi, \phi_0, \dot{\gamma}) = \lambda^2(\Delta\phi, \phi_0)\eta\dot{\gamma}_0/\dot{\gamma}\,; \qquad \eta = \mathrm{const} \geq 0, \quad \dot{\gamma}_0 = \mathrm{const} > 0. \tag{16}$$

Normalization by $\dot{\gamma}$ of the underlying medium is needed to keep viscous forces reasonable at high rates; otherwise, t_c and a are overestimated. Integrating Equation 12 and using Equation 8 in conjunction with Equation 14, Equation 15 is

$$\frac{\lambda}{\alpha}\left(1 + \frac{\lambda\eta\dot{\gamma}_0}{2\rho_0 a^2}t_c\right) = \frac{\beta}{\rho_0 ca}\left(\frac{\tau_y^3\dot{\gamma}}{18\rho_0}t_c^3\right)^{1/2} - \frac{\lambda^2\chi_0}{2\alpha a^2}t_c\left(1 + \frac{2}{5}\frac{\lambda\eta\dot{\gamma}_0}{\rho_0 a^2}t_c\right), \tag{17}$$

where an assumption similar to that used for χ_e is used for integrating η_e. Rearranging,

$$\begin{aligned}\tau_y\psi_c = \left(\frac{\tau_y^3\dot{\gamma}}{18\rho_0}t_c^3\right)^{1/2} &= \frac{\lambda\rho_0 ca}{\alpha\beta}\left\{1 + \frac{t_c}{2a^2}\left[\lambda\chi_0 + \frac{\lambda\eta\dot{\gamma}_0}{\rho_0}\left(1 + \frac{2}{5}\frac{\lambda\chi_0}{a^2}t_c\right)\right]\right\} \\ &\approx \frac{\lambda\rho_0 ca}{\alpha\beta}\left\{1 + \frac{\Xi t_c}{2a^2}\right\}, \end{aligned} \tag{18}$$

$$\Xi = \lambda(\chi_0 + \eta\dot{\gamma}_0/\rho_0). \tag{19}$$

The effective diffusivity Ξ includes thermal and nonlinear viscous effects that both instill a finite width to the shear band. Smallness of the term in Ξ proportional to $\frac{2}{5}$ relative to unity, accounting for coupling of thermal and viscous diffusion, is verified a posteriori. In terms of ψ_c, Equation 18 is, with Γ a dissipated energy,

$$\begin{aligned}&\psi_c^2 = \frac{4}{9}\frac{\tau_y\dot{\gamma}a^6}{\rho_0\Xi^3}\left(\frac{\alpha\beta\tau_y}{\lambda\rho_0 ca}\psi_c - 1\right)^3 \Leftrightarrow \Gamma^2 = \frac{\tau_y^3\dot{\gamma}a^6}{9\rho_0\Xi^3}\left(\frac{2\alpha\beta}{\lambda\rho_0 ca}\Gamma - 1\right)^3; \\ &\Gamma = \int_0^{\psi_c} \tau_0\,\mathrm{d}\psi = \frac{1}{2}\tau_y\psi_c. \end{aligned} \tag{20}$$

4. Analytical Solution

Among all possible widths $a_\star$, optimum width a should be achieved with the lowest expenditure of energy, meaning the minimum of Γ with respect to $a_\star$.[6,41,42] The same optimal width corresponds to a minimum shear band evolution time t_c.[23] If numerous bands nucleate, release waves from more rapidly growing bands arrest more slowly growing bands. If sample dimensions are not too large, a single band dominates failure. This is the case witnessed in SHPB experiments[19–21] and simulations,[17] wherein specimen failure is linked to a single primary band. Denoting $\Gamma_\star = \Gamma(a_\star)$, differentiating the second of Equation 20 gives

$$3\Gamma_\star \frac{\mathrm{d}\Gamma_\star}{\mathrm{d}a_\star} = \frac{\tau_y^3 \dot{\gamma} a_\star^5}{\rho_0 \Xi^3} \left(\frac{2\alpha\beta}{\lambda \rho_0 c a_\star} \Gamma_\star - 1 \right)^3 + \frac{\alpha\beta \tau_y^3 \dot{\gamma} a_\star^5}{\lambda c \rho_0^2 \Xi^3} \left(\frac{2\alpha\beta}{\lambda \rho_0 c a_\star} \Gamma_\star - 1 \right)^2 \left(\frac{\mathrm{d}\Gamma_\star}{\mathrm{d}a_\star} - \frac{\Gamma_\star}{a_\star} \right). \tag{21}$$

Redefining (a, Γ) as $(a_\star, \Gamma_\star)$ for which $\mathrm{d}\Gamma_\star/\mathrm{d}a_\star = 0$, Equation 21 gives the nondegenerate (i.e., $\Gamma \neq 0$) relation

$$\alpha\beta\Gamma = \lambda \rho_0 c a. \tag{22}$$

Substituting into Equation 20, optimum shear band width and matrix failure energy per unit area are, respectively,

$$a = \left(\frac{9\lambda^2 c^2 \rho_0^3 \Xi^3}{\alpha^2 \beta^2 \tau_y^3 \dot{\gamma}} \right)^{1/4}, \qquad \Gamma = \frac{\lambda \rho_0 c}{\alpha\beta} \left(\frac{9\lambda^2 c^2 \rho_0^3 \Xi^3}{\alpha^2 \beta^2 \tau_y^3 \dot{\gamma}} \right)^{1/4}. \tag{23}$$

Width in Equation 23 can be compared with Grady's original inviscid solution:[6,41]

$$\{\lambda \to 1, \beta \to 1, \Xi \to \chi_0\} \quad \Rightarrow \quad a \to [9c^2 \rho_0^3 \chi_0^3 / (\alpha^2 \tau_y^3 \dot{\gamma})]^{1/4}. \tag{24}$$

In the limit $\Delta\phi \to 0 \Rightarrow \lambda \to 1$, localization initiates from a local perturbation too small to measurably affect the stress-displacement law in Equation 9 or the energy balance in Equation 13.

Neither the linearly viscous augmentation explored briefly by Grady[6] nor the viscoplastic modification by Sheng et al.[46] retain the simplicity of the original solution as in Equation 23. Linear viscosity[6] does not seem to allow a closed-form analytical solution, and prior extensions[6,46] produce a singular solution $a \to 0$ and

$\Gamma \to 0$ as $\chi_0 \to 0$. In contrast, Equation 23 with Ξ defined in Equation 19, allows for nonzero a and Γ even in the limit of null conduction. Other microscopic dissipative mechanisms, distinct from heat flow, can preclude a near zero-width, zero-energy band. Sheng et al.[46] also consider constant β possibly differing from unity. Prior analytical models did not address porosity ϕ_0 or heterogeneity from local defects akin to λ.

It can be verified graphically that Equation 23 corresponds to a global minimum of $\Gamma_\star(a_\star)$.[6,46] As initiated by Grady,[6] the second of Equation 20 with the solution in Equation 23 can be recast as

$$2(\Gamma_\star/\Gamma)/(a_\star/a) = 1 + [(\Gamma_\star/\Gamma)^{1/3}/(a_\star/a)]^2. \tag{25}$$

Substitution of Equation 23 into governing equations of Sections 2 and 3 produces other band characteristics. Critical shear displacement δ_b, final slipped distance ψ_c, localization time t_c, final band temperature excursion θ_c, relaxation distance function $\xi(t)$, and its speed $\mathrm{d}\xi/\mathrm{d}t$ are, using Equation 23,

$$\delta_b = 2\psi_c = \frac{4\Gamma}{\tau_y} = \frac{4\lambda\rho_0 c}{\alpha\beta\tau_y}\left(\frac{9\lambda^2c^2\rho_0^3\Xi^3}{\alpha^2\beta^2\tau_y^3\dot\gamma}\right)^{1/4} = \frac{4\lambda\rho_0 c}{\alpha\beta\tau_y}a, \tag{26}$$

$$t_c = \left(\frac{18\rho_0}{\tau_y\dot\gamma}\right)^{1/3}\psi_c^{2/3} = 6\left(\frac{\lambda^2c^2\rho_0^3\Xi}{\alpha^2\beta^2\tau_y^3\dot\gamma}\right)^{1/2} = \frac{2a^2}{\Xi}, \tag{27}$$

$$\theta_c = \frac{\lambda}{\alpha}\left[1 + \frac{\eta\dot\gamma_0}{\rho_0\chi_0 + \eta\dot\gamma_0}\right]; \qquad \xi(t) = \frac{1}{12}\frac{\tau_y^2}{\rho_0\Gamma}t^2, \quad \frac{\mathrm{d}\xi}{\mathrm{d}t} = \frac{1}{6}\frac{\tau_y^2}{\rho_0\Gamma}t. \tag{28}$$

Assume in the absence of localized defects (i.e., $\lambda = 1$), temperature rise is a fraction $f_M \in (0, 1]$ of melt temperature θ_M less room temperature θ_0[15] (here, $\theta_0 = 293\,\mathrm{K}$[17]). Then α satisfies

$$\alpha = \frac{1}{f_M\theta_M}\left[1 + \frac{\eta\dot\gamma_0}{\rho_0\chi_0 + \eta\dot\gamma_0}\right], \qquad f_M = \frac{\theta_M - \theta_0}{\theta_M}. \tag{29}$$

If the effect of viscous dissipation on α is omitted,[6,46] θ can greatly exceed θ_M before localization completes, which is physically unrealistic. Note η accounts for strain-rate sensitivity of *solid* material, not viscosity of liquid metal. Latent heat of melting[10] is not included here or in other prior works.[6,46] From Equation 27, the higher-order term omitted in Equation 18, usually small in Section 5 whenever η is nonnegligible,

is

$$(2/5)(\lambda\chi_0/a^2)t_c = (4/5)[\rho_0\chi_0/(\rho_0\chi_0 + \eta\dot{\gamma}_0)]. \tag{30}$$

The expression for length of the ductile-failure process zone, ζ_b, of Grady[6] and Sheng et al.,[46] in turn based on early work of Lawn and Wilshaw,[62] is adapted to permit nominal porosity ϕ_0. The elastic shear modulus of the matrix is $\mu = \text{const}$, and that of the porous material is $\hat{\mu} = (1 - \varphi_0)\mu$. Recall dynamic strength of the matrix is τ_y, and that of the porous material is $\hat{\tau}_y = (1 - \phi_0)\tau_y$. Correspondingly, dissipated energy Equation 20 of the shear band scaled per unit area of *porous* material is $\hat{\Gamma} = (1 - \phi_0)\Gamma$. Extending Grady's model[6] and defining the average propagation speed over the kinetic history as υ_b, porosity terms cancel and

$$\zeta_b = \frac{\pi}{4}\frac{\hat{\mu}\hat{\Gamma}}{\hat{\tau}_y^2} = \frac{\pi}{4}\frac{\mu\Gamma}{\tau_y^2} = \frac{\pi}{4}\frac{\lambda\rho_0 c\mu}{\alpha\beta\tau_y^2}\left(\frac{9\lambda^2c^2\rho_0^3\Xi^3}{\alpha^2\beta^2\tau_y^3\dot{\gamma}}\right)^{1/4}, \quad \upsilon_b = \frac{\zeta_b}{t_c} = \frac{\pi}{8}\frac{\mu\Xi}{\tau_y^2}\frac{\Gamma}{a^2}. \tag{31}$$

According to Equation 31, a narrower band propagates faster than a wider band of matching energy Γ.

Grady and Kipp[23] proposed an optimum periodic band spacing of $2\xi(t_c)$ for densely packed shear bands in a shock-process zone. That expression for periodic spacing is not used here in calculations depicting SHPB experiments, wherein one dominant band leads to global stress collapse. Rather, band spacing in the current application, at lower rates than for shock, effectively equals or exceeds the gage length L of the torsion specimen. Omission of elastic waves in the rigid-plastic model (Section 2) also renders $2\xi(t_c)$-depiction of spacing less accurate at lower rates.[6]

In application of the present framework to study simple shear, the minimum strain at which localization initiates from a small perturbation is assumed to be the peak instability strain γ_p.[2,3,13,51] Assuming homogeneous adiabatic deformation up to this instability threshold, initial conditions for the localization analysis, given in Section 6 for a power-law thermo-viscoplastic solid sheared at constant rate $\dot{\gamma}$ from ambient (e.g., room) starting temperature θ_0, are

$$\theta_y = \theta(\gamma_p; \dot{\gamma}, \theta_0), \qquad \tau_y = \tau(\gamma_p; \dot{\gamma}, \theta_0)/(1 - \phi_0), \qquad t_p = \gamma_p/\dot{\gamma}, \tag{32}$$

where $t_p \leq t_0$ is the time at peak stress and τ, θ, and γ_p are given by respective Equations 42, 45, and 46.

Henceforth for clarity, the time datum is shifted so $t = 0$ corresponds to the start of the experiment when $\gamma = 0$, $\tau = 0$, and $\theta = \theta_0$. The shear band evolution model of Sections 2 and 3 spans domain $t \in [t_0, t_0 + t_c]$, where the magnitude of the process time is t_c, and $t_0 \geq t_p$. The failure time at which $\gamma = \gamma_c$ is $t_f = \gamma_c/\dot{\gamma} \geq t_p + t_c$.

Over $t \in (t_p, t_0)$, the strain field in a dynamic torsion test becomes heterogeneous, prior to the late stage of localization. Strain rate increases close to location of the pending band and decreases farther away.[14,20,21] The rigid-plastic framework of Section 2 is not designed to capture this pre-localization process, and initiation time t_0 is not known a priori. Instead, define a ratio r_0:

$$t_f = t_0 + t_c = t_p + (t_0 - t_p) + t_c = t_p + r_0 t_c, \quad r_0 = (\gamma_c - \gamma_p)/(\dot{\gamma}\, t_c) = (t_f - t_p)/t_c \geq 1. \tag{33}$$

The net post-peak strain contribution to γ_c for $t \in (t_p, t_c]$ from material outside the band is depicted as arising from a region of reduced average strain rate $\dot{\bar{\gamma}} = \dot{\gamma}/r_0$ over scaled duration $\bar{t} = t_c r_0$ such that

$$\gamma_c = \gamma_p + \varphi_b \gamma_b + (1 - \varphi_b)\dot{\bar{\gamma}}\, \bar{t} = \gamma_p + \varphi_b \gamma_b + (1 - \varphi_b)\dot{\gamma}\, t_c, \tag{34}$$

$$\gamma_b = \frac{\delta_b}{a} = \frac{4\lambda\rho_0 c}{\alpha\beta\tau_y}, \qquad \varphi_b = \frac{a}{L}. \tag{35}$$

Specimen length L necessarily affects γ_c. The volume fraction of banded material is ϕ_b, and γ_b is average shear strain supported by the band of fixed width a (i.e., displacement redistributed linearly over the width as in Figure 1). This representation of ϕ_b assumes the band traverses the circumference of the specimen, accelerating if necessary as $t \to t_f^+$. An equivalent result is obtained if the band is assumed to nucleate homogeneously with respect to y; then Equation 31 is irrelevant. Critical strain γ_c is conveniently independent from r_0, though the latter can be calculated if γ_c and γ_p are known with t_c found through Equation 27. Then from Equation 33, $t_0 = t_p + (r_0 - 1)t_c$; as $r_0 \to 1$, $t_0 \to t_p$.

A specific form of $\lambda(\Delta\phi, \phi_0)$ of Equation 10 must be prescribed. In Section 5, an exponential form proves useful to describe numerical data[17]:

$$\lambda = \exp\left[-\hat{\omega}\frac{\Delta\phi}{\phi_0}\right] = \exp\left[-\omega\left(A\frac{\Delta\phi}{\phi_0}\right)\right], \qquad \omega = \frac{\hat{\omega}}{A} = \text{const} \geq 0. \tag{36}$$

Argument $A\Delta\phi/\phi_0$ is calculated from porosity data via procedures of Section 7. The proportionality constant $A > 0$ accounting for uncertainty in $\Delta\phi/\phi_0$ (see Section 7) is absorbed into $\hat{\omega}$. Although ad hoc, Equation 36 fulfills constraints of Equation 10, has only one free parameter, and is adequate for the application in Section 5.2. Its wider validity for other materials should be studied in the future.

5. Results

5.1 Parameterization

The framework of Sections 2 through 4 is first exercised to describe dynamic finite element (FE) simulations of porous polycrystalline metals reported by Vishnu et al.[17] In these simulations, thin-walled tubes were subjected to dynamic torsion. Loading conditions mimicked SHPB experiments, albeit with periodic rather than finite boundaries to minimize edge effects and allow shear banding to occur anywhere within the gage length. Two metals were studied: commercially pure Ti and HY-100 steel. Constitutive models of the general form in Section 6 were used: power-law strain hardening, strain-rate hardening, and thermal softening. Simulations applied strain rates $\dot{\gamma}$ from 10^2/s to 10^4/s, with a majority of results presented for $\dot{\gamma} = 10^3$/s. The internal diameter, thickness, and length L of the tube were 9.5, 0.38, and 2.5 mm, respectively. Solid material was idealized as isotropic, but discrete voids were resolved in FE meshes. Representative microstructures were reconstructed based on experimental characterization of AM metals.[26] Average porosities for microstructures modeled predominantly by Vishnu et al.[17] and depicted in the current study are small, with ϕ_0 on the order of 10^{-3} or 0.1%. Simulation of a fully dense microstructure ($\phi_0 = 0$) was also reported for Ti.

A benefit of comparison versus FE results is that detailed information on many microstructures is available.[17] Drawbacks are that results are subject to limitations of underlying constitutive models, parameters, and numerical (e.g., mesh) resolution.

Heat conduction was omitted in the torsion simulations,[17] but a prior study with dynamic compression loading conditions[18] showed very small effects of heat conduction on localization behavior. Shear banding was promoted primarily by pores and thermal softening and was modulated by strain rate sensitivity. Localized flow tended to initiate at the largest pores or regions of largest local void volume fraction, with secondary localizations at smaller defects. As deformation progressed, the

dominant shear band tended to emerge over the circumference and override effects of secondary bands, leading to final failure. This concurs with the justifications by Grady and Kipp,[6,23] noted in Section 4, for the dominant shear band to follow a minimum critical-time or minimum surface-energy principle.

Critical strain γ_c at pending specimen failure tended to increase weakly with ϕ_0 and more strongly with largest pore size. In the present framework, effects of large voids or clusters of voids are modeled in a continuum-distributional sense through local concentration function $\Delta\phi$. The ratio $\Delta\phi/\phi_0$ measures the effective *spatial* increase in void fraction in the vicinity of the largest defect, where the shear band nucleates, relative to the global average ϕ_0. According to the present analysis of simple shear (e.g., no expansion or tensile pressure), the void distribution is constant in time; $\Delta\phi/\phi_0$ is an initial condition.

A mathematical definition and procedure by which defect concentration $\Delta\phi/\phi_0$, scaled by constant factor A, is calculated from the microstructure data of Vishnu et al.[17] are given in Section 7. This concentration, in turn, is used in Equation 36 to compute softening function $\lambda = 1 - \Lambda$, recalling $\lambda = 1$ corresponds to a homogeneous material. Numerical results[17] showed a modest decrease in γ_c when strain rate was increased from 10^3 to 10^4/s. For the fully dense material, a single dominant shear band formed in the center of the specimen due to symmetry. The band in this instance appeared to be wider (i.e., larger a) and delayed (larger t_c and γ_c) relative to those that emerged in porous microstructures.

Parameters entering the current analysis are given in Table 1 with supporting references. Far-field conditions—namely, τ_y, θ_y, and γ_p—are found from Equation 32 and procedures in Section 6. These conditions are reported in Table 1 for far-field strain rates of $\dot{\gamma} = 10^3$/s and $\dot{\gamma} = 10^4$/s. Parameters used in Equation 42 are converted to shear stress versus shear strain from the sourced 3-D FE constitutive implementation[17] couched in terms of effective (i.e., Von Mises) stress and strain. The viscoplasticity parameters influence τ_y, θ_y, and γ_p, but do not otherwise affect the analysis.

Only two parameters entering the analytical solution derived herein for shear band characteristics require calibration: the viscosity product $\eta\,\dot{\gamma}_0$ and the softening parameter ω entering Equation 36. The former (i.e., η) is tuned for each material to match values of γ_c in the limit of zero or very small $\Delta\phi$ from simulations[17] at

$\dot{\gamma} = \dot{\gamma}_0 = 10^3$/s. The latter (i.e., ω) is fit by regression of γ_c to simulation data[17] over a range of maximum pore sizes and average porosities (Section 7). Outcomes are discussed in Section 5.2. Recall γ_c is predicted by the current approach via Equation 34.

In most results reported subsequently, experimental values of thermal diffusivity χ_0 are used for realism, even though simulations[17] assume locally adiabatic conditions. In the present approach, thermal diffusivity can be eliminated by increasing viscosity η. If η_0 is a value of η with conduction enabled, then a default "artificial" viscosity to offset χ_0 can be included in Ξ of Equation 19:

$$\eta \to \eta_0 + \rho_0 \chi_0 / \dot{\gamma}_0, \qquad \Xi \to \lambda \eta \dot{\gamma}_0 / \rho_0. \tag{37}$$

As shown in Section 5.2, results of equal accuracy can be obtained via Equation 37 or $\chi_0 > 0$ in Equation 19.

Table 1. Properties or parameters used in calculations for Ti and HY-100 steel.

Quantity	$\dot{\gamma}$	Ti	HY-100	Definition	Reference
ρ_0 (g/cm^3)	–	4.51	7.86	density (no pores)	Vishnu et al.[17]
c (J/kg K)	–	528	473	specific heat	Vishnu et al.[17]
k_0 (W/m K)	–	19	39	conductivity	Vishnu et al.,[18] Norkett et al.[63]
θ_M (K)	–	1941	1793	melt temperature	Ishikawa et al.,[64] Norkett et al.[63]
β	–	0.9	0.9	Taylor-Quinney	Vishnu et al.[17,18]
μ (GPa)	–	43.3	76.0	shear modulus	Vishnu et al.[17]
τ_y (MPa)	10^3/s	631	629	peak flow stress	calculated (Clayton[10] solution)
	10^4/s	674	645		
θ_y (K)	10^3/s	327	338	peak temperature	calculated (Clayton[10] solution)
	10^4/s	327	338		
γ_p	10^3/s	0.16	0.32	peak applied strain	calculated (Clayton[10] solution)
	10^4/s	0.15	0.31		
$\eta \cdot \dot{\gamma}_0$ (Pa s)	–	1.22	0.65	band viscosity	calibrated, $\dot{\gamma}_0 = 10^3$/s
ω	–	0.025	0.025	defect softening	calibrated

5.2 Comparison with Data

Results of the analytical framework are first compared with simulation data of Vishnu et al.[17] In Figure 2a, critical strain γ_c versus scaled defect concentration $A\Delta\phi/\phi_0$ provides equally satisfactory regression to the data for Ti when χ_0 is enabled or when Equation 37 is used. For steel in Figure 2b, results with Equation 37 are close but not identical to those with nonzero χ_0. However, the default value of Equation 37 can be increased by 13% to give near-perfect agreement. Data from

FE simulations[17] do not include γ_c for multiple microstructures at loading rates $\dot{\gamma}$ other than 10^3/s. However, outcomes of the current analysis in Figures 2c and 2d show a slight decrease in γ_c as strain rate increases from 10^3 to 10^4/s, which is consistent with general trends reported by Vishnu et al.[17] Data are obtained from simulations[17] on the same 10 porous microstructures (i.e., same distributions of $\Delta\phi$ and ϕ_0) but with different constitutive parameters for Ti and HY-100 steel. Thus, if ω is only associated with microstructure heterogeneity, then one might expect the same value to apply regardless of properties of the fully dense homogeneous solid. This proposition is confirmed in Table 1: the same value $\omega = 0.025$ provides satisfactory descriptions of both materials.

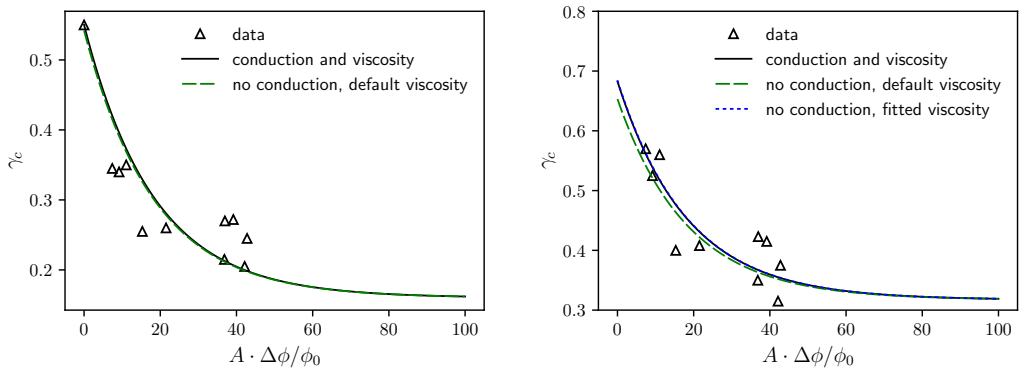

(a) Ti, 10^3/s

(b) steel, 10^3/s

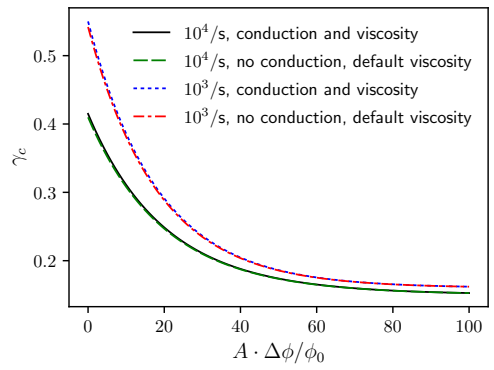

(c) Ti, two strain rates

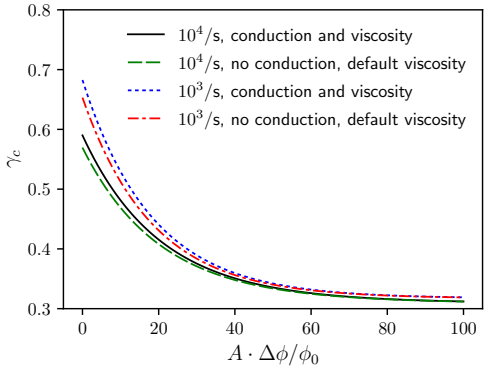

(d) steel, two strain rates

Figure 2. Critical average shear strain γ_c vs. normalized defect concentration $A\Delta\phi/\phi_0$: (a) model with and without heat conduction for Ti at $\dot{\gamma} = 10^3$/s vs. numerical simulation data[17] (b) model for HY-100 steel at $\dot{\gamma} = 10^3$/s vs. data[17] (c) model for Ti at $\dot{\gamma} = 10^3$/s and $\dot{\gamma} = 10^4$/s (d) model for HY-100 steel at $\dot{\gamma} = 10^3$/s and $\dot{\gamma} = 10^4$/s. When heat conduction is omitted, default viscosity is found from Equation 37. Fitted viscosity in (b) is tuned to 1.13 times default from Equation 37 to match result with conduction enabled.

Note also that the value of η for Ti is around 1.9 times that of HY-100 steel. This is notionally consistent with a higher macroscopic rate sensitivity m for Ti around 2.8 times that of this steel.[17]

Other quantities predicted by the present analytical solution of Section 4, using properties of Ti and HY-100 steel of Table 1, are shown in Figure 3 for the range of defect concentration $A\Delta\phi/\phi_0 \in [0, 100]$ and strain rates $\dot{\gamma}$ of 10^3 and 10^4/s. All quantities decrease with increasing local defect fraction, some more severely than others. Consistent with a 1-D spatial analysis,[6,41] for a given material, loading rate, and defect concentration, ζ_b is an order of magnitude larger than δ_b, the latter in turn an order of magnitude larger than a. Ratio θ_c/θ_M decreases from unity with increasing $\Delta\phi/\phi_0$ nearly identically for both materials and loading rates. This is a consequence of the definition of α in Equation 29, comparable θ_M for each material, and f_M similar to Grady's work.[42]

Next, predictions of the present model are compared with experimental SHPB findings, specifically test 208 of Duffy and Chi[20] on HY-100 steel at $\dot{\gamma} = 1350$/s. Properties are unchanged from Table 1 apart from $\tau_y = 631$ MPa and a slight reduction in γ_p recalculated at this strain rate via methods of Section 6. The value of λ is chosen such that γ_c perfectly matches the experimental failure strain. This steel is not described as porous in the experimental reference,[20] but like any real material, heterogeneities in the microstructure that could initiate localization are inevitable. These may include groups of grains preferentially oriented for geometric softening, weakened grain boundaries or inclusions, or regions of lower dislocation density. Torsion specimens are also prone to thickness variations whose effects could manifest in a lower shearing resistance[4,8] via $\lambda < 1$, though the boundary value problem as setup in Section 2 does not explicitly address such macroscopic geometric irregularities.

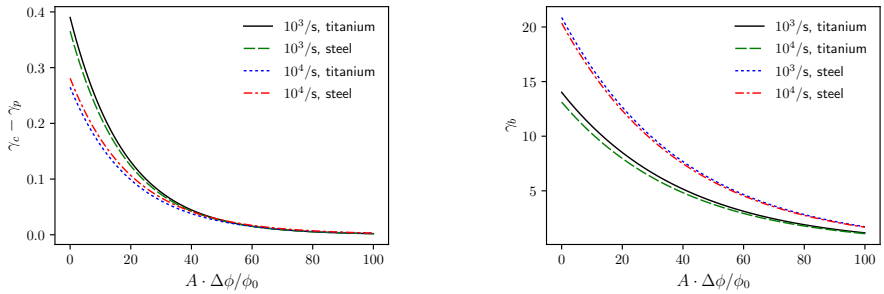

(a) critical strain past peak

(b) band strain

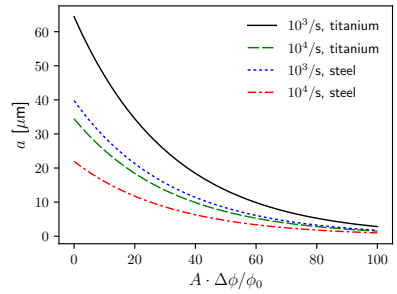

(c) band width

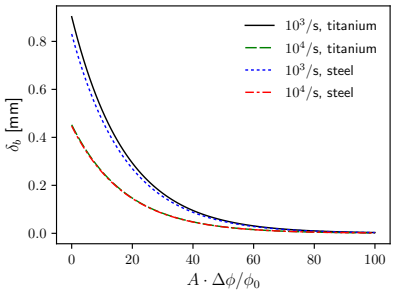

(d) band slip

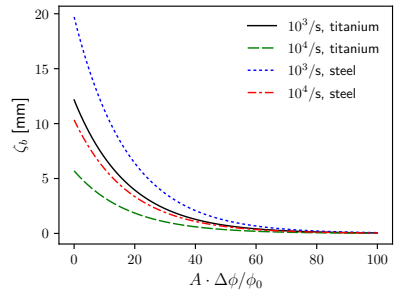

(e) zone length

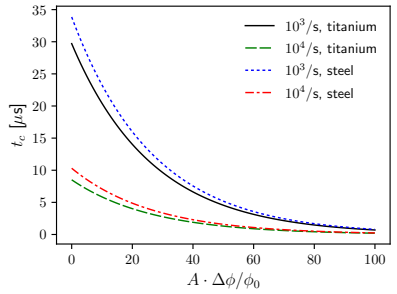

(f) growth time

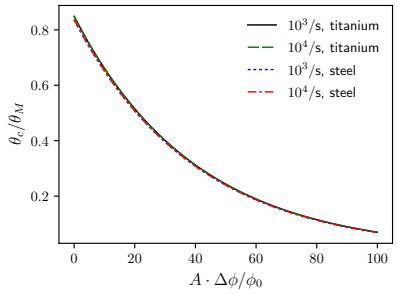

(g) homologous temperature

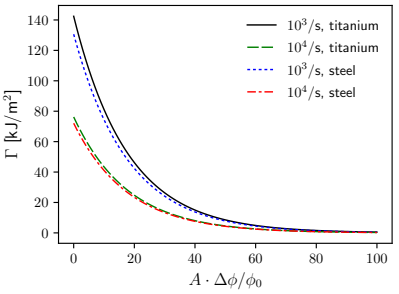

(h) band energy

Figure 3. Predicted influence of defect (excess pore) concentration $A\Delta\phi/\phi_0$ on shear band characteristics of Ti and HY-100 steel; properties of Table 1: (a) $\gamma_c - \gamma_p$ (b) γ_b (c) a (d) δ_b (e) ζ_b (f) t_c (g) θ_c (h) Γ.

Table 2. Results comparison for HY-100 steel, $\dot{\gamma} = 1350/\mathrm{s}$.

Model or experiment	τ_y (MPa)	γ_c	γ_b	a (μm)	θ_c (K)
Experiment (Duffy and Chi[20])	635	0.530	10	20[a]	575–1170
Present ($\beta = 0.9$, $\lambda = 0.8$, $\eta = 6.5 \times 10^{-4}$ kg/m)	631	0.530	16.7	27.9	1201
Grady model[6,42] ($\beta = 1$, $\lambda = 1$, $\eta = 0$)	625	0.437	35.7	9.4	1500

[a]reported width at end of experiment

Results in Table 2 compare peak stress τ_y, critical strain γ_c of Equation 34, shear band strain γ_b, shear band width a, and maximum band temperature rise θ_c among experiment,[20] the present model, and reduction of the latter to Grady's original theory[6,42] (which did not include Equation 34). The present work closely matches experimental value of τ_y and predicts the final shear band width within 40%. Shear band strain γ_b is overpredicted by 67%, temperature minimally by only 31 K. The experimental temperature measurement is prone to great uncertainty as discussed by Duffy and Chi,[20] but the upper bound was stated as significantly lower than the melt temperature (1793 K).

The original inviscid theory of Grady[6,42] gives predictions of all quantities that are less accurate, often significantly so. Shear band strain is 3.6 times the experimental result, and width under half the experimental result. Temperature rise is excessive. An even higher, and thus even more unrealistic, temperature rise would be predicted from the linearly viscous extension by Grady[6] and the viscoplastic analysis of Sheng et al.[46] In those works, viscous dissipation increases temperature beyond that of the original theory[41] (here, 1500 K with f_M of Equation 29) because $\alpha \approx 1/(\theta_M - \theta_0)$ is used therein.[6,46]

In the current theory, it is possible to achieve a lower θ_c than reported in Table 2 by decreasing f_M. However, given uncertainty in experimental thermal data, this exercise, which requires recalibration of other parameters (η, ω) for consistency, is not pursued further.

Experimental and calculated shear band widths are compared with several other analytical predictions in Table 3, for the material and loading conditions matching Table 2. Shear band widths a predicted by models of Wright and Ockendon[12] and Dinzart and Molinari,[40] respectively, for small strain-rate sensitivity exponent m, are

as follows:

$$a = \frac{2m}{1-m}\frac{k_0\theta_0}{\alpha_0 g_0 v_0}, \qquad \text{[Wright \& Ockendon]}; \tag{38}$$

$$a = 6\sqrt{2}m\frac{k_0\theta_0}{\alpha_0 g_0 v_0}, \qquad \text{[Dinzart \& Molinari]}. \tag{39}$$

Here, $v_0 = \dot{\gamma}\, h = \dot{\gamma} L/2$ is applied velocity, h is specimen half-width normal to the shear plane, g_0 is initial yield strength, and α_0 is a dimensionless thermal softening parameter. The flow rule[40] is $\tau = g_0(1 - \alpha_0\theta/\theta_0)(\dot{\gamma}/\dot{\gamma}_0)^m$. Values used in the calculation of Equations 38 and 39 for HY-100 steel from the original reference[40] reproduced in Table 3 are $v_0 = 1.68$ m/s, $g_0 = 500$ MPa, $m = 0.012$, $k_0 = 54$ W/m K, $\alpha_0 = 0.248$, and $\theta_0 = 300$ K.

As witnessed in Table 3, the present model provides the closest result to the experimental value of a. Another model due to Dodd and Bai[39] supplies a formula for a; however, this formula requires a priori knowledge of strain rate and temperature inside the band, rather than initial or far-field values, so cannot be used without further assumptions on the state of the band. Formulae of Sheng et al.[46] are not pursued due to complexity and several uncertain parameters.

Table 3. Shear band width comparison for HY-100 steel, $\dot{\gamma} = 1350/\mathrm{s}$, $L = 2h = 2.5\,\mathrm{mm}$.

Model or experiment	Eq. no.	a (μm)	Error (%)
Experiment (Duffy and Chi[20])	...	20	...
Present model	Equation 23	27.9	+39.5
Grady model[6]	...	9.4	−53.0
Dinzart-Molinari model[40]	Equation 38	8.1	−59.5
Wright-Ockendon model[12]	Equation 39	1.9	−90.5

5.3 Effects of Viscosity and Defects

The two most novel aspects of the present theory are nonlinear viscosity and consideration of localized defects. These manifest, respectively, through parameters η and ω. Keeping all other parameters fixed for those of HY-100 steel in Table 1, effects of ranges of η and ω are explored next. Strain rates $\dot{\gamma}$ of 10^3/s and 10^4/s and defect concentrations $A\Delta\phi/\phi_0$ of 10 and 40 are considered.

Outcomes for $\eta/\eta_0 \in [0, 2]$ at fixed $\omega = \omega_0$, where (η_0, ω_0) are nominal values in Table 1, are shown in Figure 4. In Figure 4a, a slight decrease in γ_c occurs with increasing η at small η/η_0, followed by a gradual increase thereafter. This unexpected

behavior at small η/η_0 is a result of the assumed form of nonlinear coupling of viscosity to thermal softening in Equation 29. In this regime, thermal softening from viscous dissipation outweighs stiffening from viscous drag. In numerical simulations,[17] increasing strain-rate sensitivity m reduced the strain γ_p at peak stress and influenced γ_c. The present analysis uses fixed parameters for Equation 42 needed only to define the initial far-field conditions θ_y, τ_y, and γ_p. Variations in n, ν, and m have not been considered here.

Effects of η are more pronounced at smaller $\Delta\phi/\phi_0$. With increasing viscosity, shear band strain γ_b decreases sharply initially, then slowly plateaus in Figure 4b. The shear band width increases in a nearly linear fashion with η/η_0 in Figure 4c; the slope decreases with increasing applied strain rate and increasing defect content. The magnitudes of slip in the band, length of the process zone, and surface energy of the band in respective Figures 4d, 4e, and 4h all follow similar trends to γ_c. Critical time t_c shows similar nonmonotonicity, but the effect of strain rate is stronger.

Temperature rise in Figure 4g is independent of η and $\dot{\gamma}$, but it is lower in the more defective, more brittle material ($A\Delta\phi/\phi_0 = 40$). A similar result was found by the author[10] using a completely different analysis of torsion of a different steel, wherein softening from damage and fracture precluded extreme temperature rise in the band.

Outcomes for $\omega/\omega_0 \in [0, 2]$ at fixed $\eta = \eta_0$ are reported in Figure 5. All predicted quantities decrease with increasing defect-softening parameter ω. Rates of decrease are logically more pronounced when $A\Delta\phi/\phi_0$ is increased, here from 10 to 40. Critical strain in Figure 5a decreases modestly as strain rate increases from 10^3 to 10^4/s, whereas the effect of $\dot{\gamma}$ on γ_b is nearly negligible in Figure 5b. Shear band width a in Figure 5c, slipped distance δ_b in Figure 5d, process zone length ζ_b in Figure 5e, growth time t_c in Figure 5f, and surface energy Γ in Figure 5h all witness similar trends with changes in ω, $\dot{\gamma}$, and $\Delta\phi/\phi_0$. Terminal band temperature in Figure 5g is independent of applied strain rate $\dot{\gamma}$, but it does decrease with increased defect-softening.

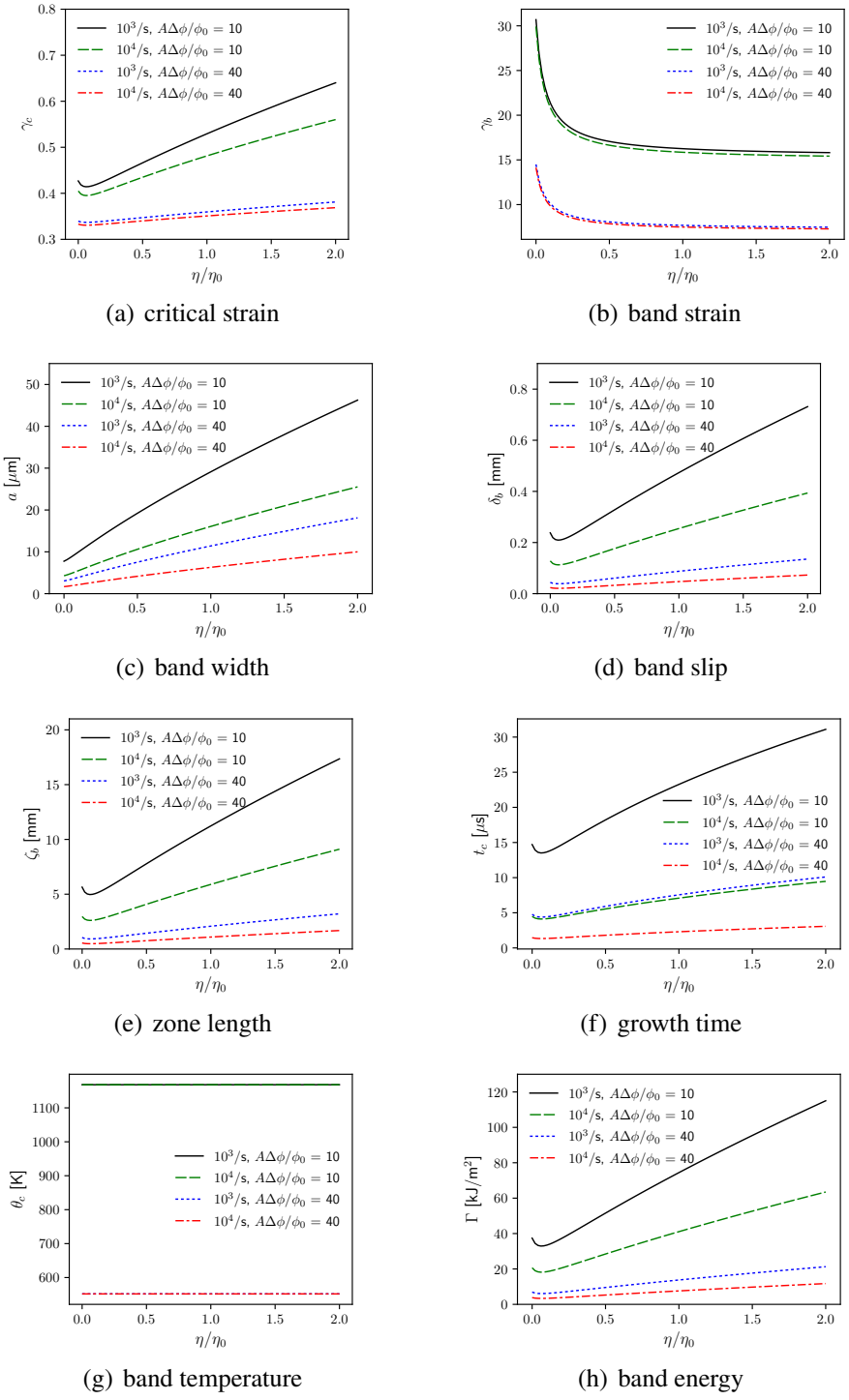

(a) critical strain (b) band strain

(c) band width (d) band slip

(e) zone length (f) growth time

(g) band temperature (h) band energy

Figure 4. Influence of viscosity η on shear band characteristics, two defect concentrations $\Delta\phi/\phi_0$, $\eta_0 = 6.5 \times 10^{-4}$kg/m, properties for HY-100 steel of Table 1: (a) γ_c (b) γ_b (c) a (d) δ_b (e) ζ_b (f) t_c (g) θ_c (h) Γ.

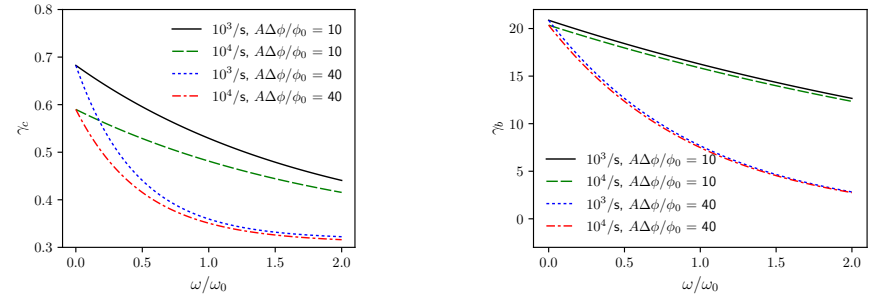

(a) critical strain (b) band strain

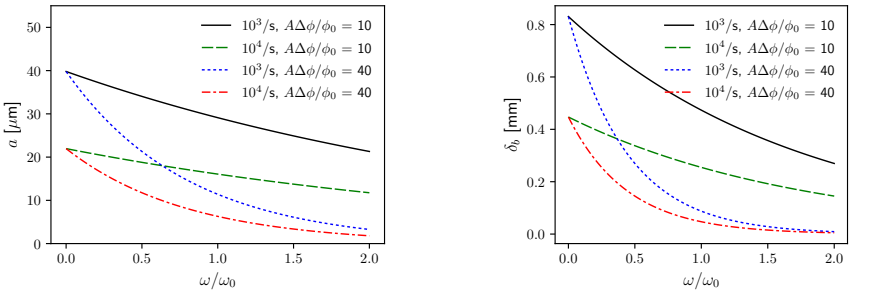

(c) band width (d) band slip

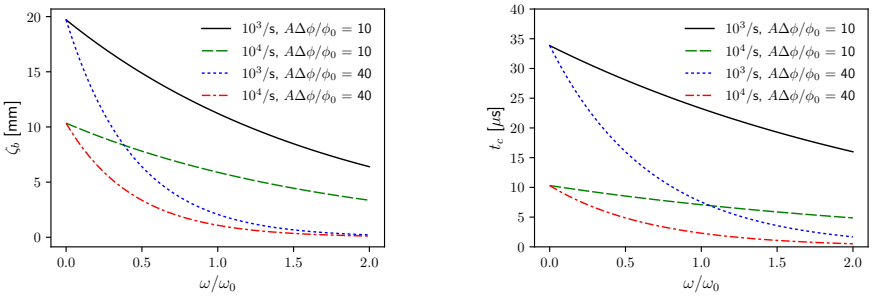

(e) zone length (f) growth time

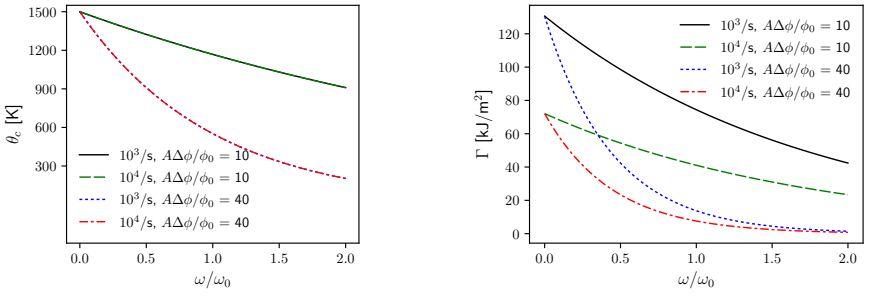

(g) band temperature (h) band energy

Figure 5. Influence of degradation factor ω on shear band characteristics, two defect concentrations $\Delta\phi/\phi_0$, $\omega_0 = 0.025$, other properties for HY-100 steel of Table 1: (a) γ_c (b) γ_b (c) a (d) δ_b (e) ζ_b (f) t_c (g) θ_c (h) Γ.

5.4 Discussion

As shown in Section 5.2, the present framework with viscosity and defect susceptibility enables a closer depiction of shear band width a, and other quantities to a limited extent, than prior analytical models. This benefit suffers the cost of the additional parameter η for nonlinear viscosity and the function λ for effects of local defects, or more broadly, microstructure heterogeneity.

In the present application, η and the constant ω entering λ of Equation 36 are obtained by fitting critical strain γ_c to numerical data.[17] A limitation is that comparison to data in Figure 2 must be viewed as calibration rather than validation. The shear band width a in Tables 2 and 3, however, is a model prediction, rather than calibration, as are shear band strain γ_b and temperature θ_c in the former. Improved agreement with experiment for these quantities relative to past models is promising.

If γ_c is unknown or of no concern, and if a is measured experimentally, parameters can be obtained using an alternative sequence. From Equation 23 for a with Equation 29 for α, an implicit relation for viscosity η and heterogeneity function λ can be derived if a is known:

$$\frac{[\lambda(\chi_0 + \eta\dot{\gamma}_0/\rho_0)]^5}{(\chi_0 + 2\eta\dot{\gamma}_0/\rho_0)^2} = \frac{\beta^2\tau_y^3\dot{\gamma}}{9c^2\rho_0^3 f_M^2\theta_M^2}a^4. \tag{40}$$

If a material were perfectly homogeneous—possible in simulations,[17] but not real experiments—then $\lambda = 1$ and η can be calculated from Equation 40 by simple numerical iteration.

The nonlinear viscosity η or η_e, physically correlated to strain-rate dependence of material response in the shear band, regularizes the solution in a manner analogous to conduction. Both prevent a zero-width band. Inertia coupled to far-field strain rate $\dot{\gamma} > 0$ prohibits the band from having infinite width.[6] Not pursued here, it might be possible to augment governing equations with additional regularization in a phase field approach, where gradients in an order parameter for ductile damage influence width of the band.[65] In that case, numerical solutions would seem necessary.

The constitutive response function in Equation 9 is not the only physically viable option. More generally, stress supported by the slip band could obey, with $\hat{k}, \hat{l}, \hat{n}$, and

$\hat{m}$ nonnegative constants,

$$\tau = (1-\phi_0)^{\hat{k}}\left(\left\{1-(\alpha\Delta\theta)^{\hat{l}}-\Lambda\left[\left(\frac{\psi}{\psi_c}\right)^{\hat{p}}\left(\frac{\psi}{\epsilon_0 a}\right)^{1-\hat{p}}\right]^{\hat{n}}\right\}\tau_y+\eta_e\left[\frac{\dot{\psi}}{a^{\hat{q}}a_0^{1-\hat{q}}}\right]^{\hat{m}}\right). \quad (41)$$

Other constants are $\hat{p} \in [0,1]$, $\hat{q} \in [0,1]$, $\epsilon_0 > 0$, and $a_0 > 0$, the latter with dimensions of length. In the current work, $\hat{k} = \hat{l} = \hat{n} = 1$ giving the simplest linear softening from initial porosity, temperature rise, and damage degradation. Also, $\hat{m} = 2$ furnishes quadratic viscosity enabling the aforementioned regularization. Other realistic choices might be $\hat{l} > 1$ and $\hat{n} > 1$, the former accounting for rapid strength loss as melting is approached, the latter expected for severe nonlinear softening from void linking and coalescence at large deformation.[66] The current choice $\hat{p} = 1$ treats the degrading surface, with linear decay ($\hat{n} = 1$), similar to a cohesive zone with sliding displacement ψ undergoing shear fracture[67,68] used elsewhere to model shear banding to ductile fracture.[69] Perhaps equally realistic, $\hat{p} = 0$ would degrade strength according to strain ψ/a, where ϵ_0 is a normalizing strain to avoid arbitrary failure at $\psi = a$ as $\Lambda \to 1$. This approach suffers from a need to calibrate ϵ_0 to data. Current prescription $\hat{q} = 1$ couples slip rate $\dot{\psi}$ to band width a, increasing its contribution to energy Γ with decreasing a. Choice $\hat{q} = 0$ would align more closely with a cohesive zone, but the regularizing effect from coupling would vanish. Finally, choices of $\hat{k}, \hat{l}, \hat{n}, \hat{m}, \hat{p}$, and $\hat{q}$ different from those in this work usually do not enable analytical solutions to the governing equations.

Nonlinearity admitted by power laws in Equation 41 might be more physically realistic, but conversely may require more parameters and preclude closed-form solutions. Transparency of solutions is compromised if numerical methods are needed. Note that the additional parameters or constants exclusively appearing in Equation 41 are excluded, for brevity, from the list of symbols at the end of this report.

The greatest source of uncertainty, and thus most severe deficiency, of the present framework, is the function λ. The exponential form Equation 36, or ranges of ω, should not be arbitrarily generalized to all porous microstructures. Furthermore, the defect concentration $\Delta\phi/\phi_0$ defined in Section 7 is pragmatically restricted to small average porosities ϕ_0 (e.g., $\phi < 1$ requires $\phi_0 \lesssim 1\%$ if $\Delta\phi/\phi_0 \lesssim 100$ as explored in Section 5.2). Experimental and/or numerical simulation data on shear band characteristics such as strain or time to failure versus extreme-value statistics of structural or state

features[70] that influence localization (e.g., distributions of porosity,[26,28,71] grain orientations,[7] weakening inclusions,[72] and dynamically recrystallized grains[53]) are required to inform a more universal, and more stringently validated, function λ broadly relevant to viscoplastic polycrystals. Like any isotropic continuum plasticity-damage approach,[2,16,28,29,38] effects of discrete defects and individual grains are unavoidably smeared into homogenized properties and statistical representations, even as void or grain sizes can affect critical strains and shear band widths.[17]

Thermodynamics and λ could be extended to explicitly capture mechanisms such as variable fraction of energy of cold work[57,59] and DRX,[52,53,58] but some detail must likely be compromised to enable simple and useful closed-form expressions. Extension to loading different from simple shear is also needed for wider relevance. Porosity should evolve more strongly in tension or compression.[30]

However, given λ and its limitations, the present research does provide a tractable framework, motivated by fundamental mechanics principles and with closed-form analytical expressions, enabling quantification and exploration of effects of defects and other material properties (e.g., yield strength, density, thermal diffusivity, viscosity) on features of shear bands, extending the seminal works of Grady and Kipp.[6,23,41,42,45] Tradeoffs among variations in λ (e.g., pores arising from contemporary AM techniques) and other physical properties can be optimized to mitigate shear banding by increasing time to collapse t_c or shear band resistance energy Γ, for example.

6. Conditions at Initial Instability

Denote shear stress, shear strain, shear strain rate, and temperature by τ, γ, $\dot{\gamma}$, and θ. Consider a power-law flow rule for an isotropic rigid-viscoplastic solid[4,8,31] ($\gamma :=$ total $\approx$ plastic shear):

$$\tau(\gamma, \dot{\gamma}, \theta; \phi_0) = (1 - \phi_0) g_0 \left(1 + \frac{\gamma}{\gamma_0}\right)^n \left(\frac{\theta}{\theta_0}\right)^\nu \left(\frac{\dot{\gamma}}{\dot{\gamma}_0}\right)^m . \tag{42}$$

Average porosity is ϕ_0, assumed constant here. Linear strength reduction by the factor $1 - \phi_0$ is standard among ductile plasticity-damage models when ϕ_0 is small relative to unity.[38,55,60,61] Strain hardening exponent n is usually positive, thermal softening exponent ν usually negative. Rate sensitivity is $m > 0$, reference temperature is θ_0, and $\gamma_0 > 0$ and $\dot{\gamma}_0 > 0$ are constants. Reference yield stress is the constant $g_0 > 0$. Under simple shear deformation, an insulated homogeneous material has spatially

constant γ and θ fields and obeys the local energy and mass balances

$$(1-\phi_0)\rho_0 c = \beta\tau\dot{\gamma}, \qquad \rho = (1-\phi_0)\rho_0. \tag{43}$$

Mass density of the incompressible matrix material without voids is $\rho_0 > 0$, specific heat per unit mass is $c > 0$, and the Taylor-Quinney factor is $\beta \geq 0$, all simply constants.

Substituting Equation 42 into Equation 43, eliminating the factor $1-\phi_0$, and defining $c_V = \rho_0 c$ the specific heat per unit volume,

$$\mathrm{d}\theta = \frac{\beta g_0}{c_V}\left(1+\frac{\gamma}{\gamma_0}\right)^n \left(\frac{\theta}{\theta_0}\right)^\nu \left(\frac{\dot{\gamma}}{\dot{\gamma}_0}\right)^m \mathrm{d}\gamma. \tag{44}$$

For constant $\dot{\gamma}$, Equation 44 is integrated for $\theta = \theta(\gamma)$ by separation of variables[4,8] with $\theta_i = \theta(0)$:

$$\begin{aligned} \theta^{-\nu}\mathrm{d}\theta &= \frac{\beta g_0}{c_V \theta_0^\nu}\left(1+\frac{\gamma}{\gamma_0}\right)^n \left(\frac{\dot{\gamma}}{\dot{\gamma}_0}\right)^m \mathrm{d}\gamma \quad \Rightarrow \\ \theta(\gamma) &= \left[\theta_i^{1-\nu} + \frac{(1-\nu)\beta g_0 \gamma_0}{(1+n)c_V\theta_0^\nu}\left(\frac{\dot{\gamma}}{\dot{\gamma}_0}\right)^m \left\{\left(1+\frac{\gamma}{\gamma_0}\right)^{1+n} - 1\right\}\right]^{\frac{1}{1-\nu}}. \end{aligned} \tag{45}$$

Insertion of Equation 45 into Equation 42 gives a stress-strain function $\tau = \tau(\gamma)$ at fixed $\dot{\gamma}$ and ϕ_0. Minimum strain at which localization initiates from a small perturbation is identified with the peak instability strain γ_p.[2,3,13,51] In simple shear, γ_p is γ for which $\mathrm{d}\tau/\mathrm{d}\gamma = 0$ (i.e., where $\tau(\gamma)$ attains a local maximum). When $\theta_i = \theta_0$, the following implicit solution for instability strain γ_p is derived[10]:

$$\gamma_p = \underset{\gamma\geq 0}{\arg 0}\left[\frac{n}{\nu A_p} + \frac{(1+\frac{\gamma}{\gamma_0})^{1+n}}{1+A_p(\frac{1-\nu}{1+n})\{(1+\frac{\gamma}{\gamma_0})^{1+n}-1\}}\right], \qquad A_p = \frac{\beta g_0 \gamma_0}{c_V\theta_0}\left(\frac{\dot{\gamma}}{\dot{\gamma}_0}\right)^m. \tag{46}$$

7. Porosity Data and Defect Concentrations

Average porosity ϕ_0, scaled defect concentration $A\Delta\phi/\phi_0$, and critical strain γ_c for Ti and HY-100 steel are obtained from numerical data on 10 realizations R1, . . ., R10 of AM microstructure INC1Z of Vishnu et al.[17] Values of ϕ_0 are sourced from Table 3 of Vishnu et al.[17] Critical strains at localization γ_c for each realization and material are from Figure 6(b) of Vishnu et al.[17] Values are collected in Table 4.

Results of FE simulations[17] show a decrease in γ_c with increasing ϕ_0 and increasing D_m, where D_m is maximum diameter of all spherical voids in a realization. However, D_m and ϕ_0 are not uncorrelated: data suggest a general increase in D_m with increasing ϕ_0. If sizes obey a random distribution, the probability of a larger void increases as their number per unit volume n_v increases.

Less correlation with ϕ_0 is attained when a normalized defect concentration $A\Delta\phi/\phi_0$ is used:

$$A\frac{\Delta\phi}{\phi_0} = \begin{cases} (\phi_m - \phi_0)/\phi_0 = \frac{\pi}{6} n_v D_m^3/\phi_0 - 1, & [\phi_0 > 0, \Delta\phi \in (0, 1-\phi_0)] \\ 0, & [\Delta\phi = 0]. \end{cases} \tag{47}$$

Proportionality constant $A > 0$ accounts for uncertainty in the true porosity where the shear band nucleates. Limits in Equation 47 restrict maximum local porosity to $\phi_m < 1$ and enforce a zero value when perturbations vanish, regardless of ϕ_0. For the former, a maximum $\Delta\phi/\phi_0 \approx 100$ necessitates $\phi_0 \lesssim 1\,\%$. Values in Table 4 of this report are calculated using ϕ_0, D_m and n_v from Table 3 of Vishnu et al.[17]

Average porosity ϕ_0 is not an appropriate influencing function for localization susceptibility in the current model. In the limit that pores are infinitesimal and homogeneously distributed, τ_y should be uniformly reduced (e.g., by a factor of $1 - \phi_0$), but no impetus exists for localization at any one location.

In the simulated microstructures,[17] voids are randomly distributed in each realization with sizes following a log-normal distribution. A similar description holds for INC1XY microstructure from AM in a related reference.[73] There, modeled specimens were discretized into 16 domains with local porosity calculated for each; see Figure 5 of Nieto-Fuentes et al.[73] Large voids correlate with regions of highest local porosity, in agreement with Equation 47. However, Equation 47 implicitly assumes voids are uniformly, rather than randomly, distributed, and it omits possible clustering. To

account for this uncertainty, unknown parameter A is introduced, which is absorbed into fitting constant $\hat{\omega}$ in Equation 36. Comparison with local porosity quoted in the cited references on AM microstructures[17,73] suggests $A > 1$ (i.e., the right side of Equation 47 overestimates local pore concentration).

Critical strain γ_c for each realization depends on its particular distribution of void locations and sizes. However, detailed spatial data on void distributions for all 10 realizations are not available from Vishnu et al.,[17] only their average porosity, void number and number density, and maximum diameter. Any estimate of $\Delta\phi/\phi_0$ for a *specific* realization is limited to this available published information.

Table 4. Porosity and critical strain γ_c at $\dot{\gamma} = 10^3/\mathrm{s}$: realizations R1, . . . , R10 of Vishnu et al.[17]

Quantity	R1	R2	R3	R4	R5	R6	R7	R8	R9	R10
ϕ_0 (%)	0.075	0.039	0.059	0.073	0.046	0.114	0.06	0.043	0.046	0.132
$A \cdot \Delta\phi/\phi_0$	21.5	37.0	42.8	15.3	7.4	42.1	9.2	39.2	11.1	36.8
γ_c, Ti[a]	0.26	0.27	0.245	0.255	0.345	0.205	0.34	0.27	0.35	0.215
γ_c, HY-100	0.41	0.425	0.375	0.4	0.57	0.315	0.525	0.415	0.56	0.35

[a] $\gamma_c = 0.55$ for $\Delta\phi = 0$

8. Conclusions

The present report advances pioneering analytical modeling of shear band evolution by Grady and Kipp to include nonlinear viscous effects and initial defects. Non-Newtonian viscosity delays stress collapse and widens the band similarly to heat conduction. Local defects accelerate collapse, narrow the band, and reduce temperature rise. Simplifying idealizations allow calibration to, and comparison with, dynamic torsion data from numerical and experimental studies on porous and fully dense metals.

Upon introduction of only two calibrated parameters, the presently derived formulae better match experimental trends for critical strain, local band strain, local temperature, and shear band thickness than the original rate-independent formulae of Grady and formulae for shear band width derived in past analytical models. Unlike the current treatment, none of these prior formulae included quantitative measures of defects such as porosity.

This work establishes a basic framework within which effects of processing defects, as often arising in contemporary AM technologies, on failure by shear banding

in rate-sensitive materials can be analyzed. The need for more experimental and numerical data relating local defect distributions in heterogeneous microstructures to the onset and physical characteristics of shear bands has been emphasized. Such information could be used to enhance validation and potentially improve predictive capabilities of the analytical framework.

9. References

1. Clayton J. Analytical shear-band process zone model incorporating nonlinear viscous effects and initial defects. Journal of Applied Mechanics. 2025;92:091009.
2. Wright T. The physics and mathematics of adiabatic shear bands. Cambridge University Press; 2002.
3. Yan N, Li Z, Xu Y, Meyers M. Shear localization in metallic materials at high strain rates. Progress in Materials Science. 2021;119:100755.
4. Molinari A, Clifton R. Analytical characterization of shear localization in thermoviscoplastic materials. Journal of Applied Mechanics. 1987;54:806–812.
5. Wright T, Ockendon H. A scaling law for the effect of inertia on the formation of adiabatic shear bands. International Journal of Plasticity. 1996;12:927–934.
6. Grady D. Properties of an adiabatic shear-band process zone. Journal of the Mechanics and Physics of Solids. 1992;40:1197–1215.
7. Molinari A. Shear band analysis. Solid State Phenomena. 1988;3–4:447–467.
8. Clayton J. Analysis of shear localization in viscoplastic solids with pressure-sensitive structural transformations. Journal of the Mechanics and Physics of Solids. 2024;193:105880.
9. Arriaga M, Waisman H. Combined stability analysis of phase-field dynamic fracture and shear band localization. International Journal of Plasticity. 2017;96:81–119.
10. Clayton J. Analysis of adiabatic shear coupled to ductile fracture and melting in viscoplastic metals. arXiv preprint. 2025;arXiv:2502.10625.
11. Needleman A. Material rate dependence and mesh sensitivity in localization problems. Computer Methods in Applied Mechanics and Engineering. 1988;67:69–85.
12. Wright T, Ockendon H. A model for fully formed shear bands. Journal of the Mechanics and Physics of Solids. 1992;40:1217–1226.
13. Shawki T. Necessary and sufficient conditions for the onset of shear strain localization in thermal viscoplastic materials. University of Illinois; 1988. Report No.: TAM-R-489.

14. Cherukuri H, Shawki T. An energy-based localization theory: I. Basic framework. International Journal of Plasticity. 1995;11:15–40.

15. Zhou F, Wright T, Ramesh K. The formation of multiple adiabatic shear bands. Journal of the Mechanics and Physics of Solids. 2006;54:1376–1400.

16. Kubair D, Ramesh K, Swaminathan P. Effect of shear-void-growth softening on adiabatic shear-band-spacing in ductile metals. Acta Mechanica. 2015;226:4189–4206.

17. Vishnu A, Nieto-Fuentes J, Rodriguez-Martinez J. Shear band formation in porous thin-walled tubes subjected to dynamic torsion. International Journal of Solids and Structures. 2022;252:111837.

18. Vishnu A, Marvi-Mashhadi M, Nieto-Fuentes J, Rodriguez-Martinez J. New insights into the role of porous microstructure on dynamic shear localization. International Journal of Plasticity. 2022;148:103150.

19. Cho K, Chi Y, Duffy J. Microscopic observations of adiabatic shear bands in three different steels. Metallurgical Transactions A. 1990;21:1161–1175.

20. Duffy J, Chi Y. On the measurement of local strain and temperature during the formation of adiabatic shear bands. Materials Science and Engineering A. 1992;157:195–210.

21. Fellows N, Harding J. Localization of plastic deformation during high strain rate torsion testing of rolled homogeneous armour. Journal of Strain Analysis for Engineering Design. 2001;36:197–210.

22. Xu Y, Zhang J, Bai Y, Meyers M. Shear localization in dynamic deformation: microstructural evolution. Metallurgical and Material Transactions A. 2008;39:811–843.

23. Grady D, Kipp M. The growth of unstable thermoplastic shear with application to steady-wave shock compression in solids. Journal of the Mechanics and Physics of Solids. 1987;35:95–118.

24. Slotwinski J, Garboczi E, Hebenstreit K. Porosity measurements and analysis for metal additive manufacturing process control. Journal of Research of the National Institute of Standards and Technology. 2014;119:494–528.

25. Ning J, Sievers D, Garmestani H, Liang S. Analytical modeling of part porosity in metal additive manufacturing. International Journal of Mechanical Sciences. 2020;172:105428.

26. Marvi-Mashhadi M, Vaz-Romero A, Sket F, Rodriguez-Martinez J. Finite element analysis to determine the role of porosity in dynamic localization and fragmentation: application to porous microstructures obtained from additively manufactured materials. International Journal of Plasticity. 2021;143:102999.

27. Dodd B, Atkins A. Flow localization in shear deformation of void-containing and void-free solids. Acta Metallurgica. 1983;31:9–15.

28. Batra R, Jin X. Analysis of dynamic shear bands in porous thermally softening viscoplastic materials. Archive of Mechanics. 1994;46:13–36.

29. Nahshon K, Hutchinson J. Modification of the Gurson model for shear failure. European Journal of Mechanics A Solids. 2008;27:1–17.

30. Silva M da, Ramesh K. The rate-dependent deformation and localization of fully dense and porous Ti-6Al-4V. Materials Science and Engineering A. 1997;232:11–22.

31. Fressengeas C, Molinari A. Instability and localization of plastic flow in shear at high strain rates. Journal of the Mechanics and Physics of Solids. 1987;35:185–211.

32. Giovanola J. Adiabatic shear banding under pure shear loading I. Direct observation of strain localization and energy dissipation measurements. Mechanics of Materials. 1988;7:59–71.

33. Schoenfeld S, Wright T. A failure criterion based on material instability. International Journal of Solids and Structures. 2003;40:3021–3037.

34. Fermen-Coker M. Implementation of Schoenfeld-Wright failure criterion into a three-dimensional adiabatic shear band model in CTH. Army Research Laboratory (US); 2004. Report No.: ARL-TR-3284.

35. Bronkhorst C, Cerreta E, Xue Q, Maudlin P, Mason T, Gray G. An experimental and numerical study of the localization behavior of tantalum and stainless steel. International Journal of Plasticity. 2006;22:1304–1335.

36. Mourad H, Bronkhorst C, Livescu V, Plohr J, Cerreta E. Modeling and simulation framework for dynamic strain localization in elasto-viscoplastic metallic materials subject to large deformations. International Journal of Plasticity. 2017;88:1–26.

37. Bronkhorst C, Hansen B, Cerreta E, Bingert J. Modeling the microstructural evolution of metallic polycrystalline materials under localization conditions. Journal of the Mechanics and Physics of Solids. 2007;55:2351–2383.

38. Gurson A. Continuum theory of ductile rupture by void nucleation and growth. Journal of Engineering Materials and Technology. 1977;99:2–15.

39. Dodd B, Bai Y. Width of adiabatic shear bands formed under combined stresses. Materials Science and Technology. 1989;5:557–559.

40. Dinzart F, Molinari A. Structure of adiabatic shear bands in thermo-viscoplastic materials. European Journal of Mechanics A Solids. 1998;17:923–938.

41. Grady D. Dynamics of adiabatic shear. Journal de Physique IV. 1991;1:653–660.

42. Grady D. Dissipation in adiabatic shear bands. Mechanics of Materials. 1994;17:289–293.

43. Mott N. Fragmentation of shell cases. Proceedings of the Royal Society of London A. 1947;189:300–308.

44. Kipp M, Grady D. Dynamic fracture growth and interaction in one dimension. Journal of the Mechanics and Physics of Solids. 1985;33:399–415.

45. Grady D, Kipp M. The growth of inhomogeneous thermoplastic shear. Journal de Physique Colloques. 1985;46:291–298.

46. Sheng DL, Chen Y, Zhou FH, Dai LH. Growth of thermoplastic shear band. Journal of Materials Research and Technology. 2024;33:4783–4795.

47. Chiou S, Tsai H, Lee W. Effects of strain rate and temperature on the deformation and fracture behaviour of titanium alloy. Materials Transactions. 2007;48:2525–2533.

48. Sadjadpour A, Rittel D, Ravichandran G, Bhattacharya K. A model coupling plasticity and phase transformation with application to dynamic shear deformation of iron. Mechanics of Materials. 2015;80:255–263.

49. Benson D. Explicit Finite Element Methods for Large Deformation Problems in Solid Mechanics. Encyclopedia of Computational Mechanics. E Stein, R de Borst, T Hughes, editors. Vol. 2. John Wiley and Sons; 2007. Chap. 25, p. 1–43.

50. Mattsson A, Rider W. Artificial viscosity: back to the basics. International Journal for Numerical Methods in Fluids. 2015;77:400–417.

51. Anand L, Kim K, Shawki T. Onset of shear localization in viscoplastic solids. Journal of the Mechanics and Physics of Solids. 1987;35:407–429.

52. Chen HS, Qi W, Chen M, Yang H, Zhu S, Zeng Q. Estimation of energy dissipation during dynamic shear band evolution. International Journal of Solids and Structures. 2025;309:113202.

53. Rittel D, Landau P, Venkert A. Dynamic recrystallization as a potential cause for adiabatic shear failure. Physical Review Letters. 2008;101:165501.

54. Zhu Z, Batra R. Consideration of phase transformations in the study of shear bands in a dynamically loaded steel block. Journal of Engineering Materials and Technology. 1992;114:368–377.

55. Clayton J. Nonlinear mechanics of crystals. Springer; 2011.

56. Clayton J. Dynamic plasticity and fracture in high density polycrystals: constitutive modeling and numerical simulation. Journal of the Mechanics and Physics of Solids. 2005;53:261–301.

57. Rittel D, Wang Z, Merzer M. Adiabatic shear failure and dynamic stored energy of cold work. Physical Review Letters. 2006;96:075502.

58. Longere P. Respective/combined roles of thermal softening and dynamic recrystallization in adiabatic shear band initiation. Mechanics of Materials. 2018;117:81–90.

59. Kunda S, Schmelzer N, Pedgaonkar A, Rees J, Dunham S, Lieou C, Langbaum J, Bronkhorst CA. Study of the thermomechanical behavior of single-crystal and polycrystal copper. Metals. 2024;14:1086.

60. Becker R, Needleman A, Richmond O, Tvergaard V. Void growth and failure in notched bars. Journal of the Mechanics and Physics of Solids. 1988;36:317–351.

61. Clayton J, Lloyd J. A dynamic finite-deformation constitutive model for steels undergoing slip, twinning, and phase changes. Journal of Dynamic Behavior of Materials. 2021;7:217–247.

62. Lawn B, Wilshaw R. Indentation fracture: principles and applications. Journal of Materials Science. 1975;10:1049–1081.

63. Norkett J, Semple J, Bechetti D, Zhang W, Fisher C. Temperature-dependent material property database for marine steels–part 6: HY-100. Naval Surface Warfare Center Carderock (US); 2023. Report No.: NSWCCD-61-TR-2023/13.

64. Ishikawa T, Paradis PF, Okada J, Watanabe Y. Viscosity measurements of molten refractory metals using an electrostatic levitator. Measurement Science and Technology. 2012;23:025305.

65. Zeng Q, Wang T, Zhu S, Chen H, Fang D. A rate-dependent phase-field model for dynamic shear band formation in strength-like and toughness-like modes. Journal of the Mechanics and Physics of Solids. 2022;164:104914.

66. Tvergaard V. Material failure by void growth to coalescence. Advances in Applied Mechanics. 1989;27:83–151.

67. Falk M, Needleman A, Rice J. A critical evaluation of cohesive zone models of dynamic fracture. Journal de Physique IV. 2001;11:5–43.

68. Clayton J. Modeling dynamic plasticity and spall fracture in high density polycrystalline alloys. International Journal of Solids and Structures. 2005;42:4613–4640.

69. Gu T, Wang Z. A strain rate-dependent cohesive zone model for shear failure of hat-shaped specimens under impact. Engineering Fracture Mechanics. 2022;259:108145.

70. Zhang Y, Chen N, Bronkhorst C, Cho H, Argus R. Data-driven statistical reduced-order modeling and quantification of polycrystal mechanics leading to porosity-based ductile damage. Journal of the Mechanics and Physics of Solids. 2023;179:105386.

71. Sun W, Andrade J, Rudnicki J, Eichhubl P. Connecting microstructural attributes and permeability from 3D tomographic images of in situ shear-enhanced compaction bands using multiscale computations. Geophysical Research Letters. 2011;38.

72. Karim M, Kadau K, Narasimhachary S, Radaelli F, Amann C, Dayal K, Silling S, Germann T. Crack nucleation from non-metallic inclusions in aluminum alloys described by peridynamics simulations. International Journal of Fatigue. 2021;153:106475.

73. Nieto-Fuentes J, Jacques N, Marvi-Mashhadi M, Nsouglo K, Rodriguez-Martinez J. Modeling dynamic formability of porous ductile sheets subjected to biaxial stretching: actual porosity versus homogenized porosity. International Journal of Plasticity. 2022;158:103418.

List of Symbols, Abbreviations, and Acronyms

TERMS

1-D	one-dimensional
2-D	two-dimensional
3-D	three-dimensional
AM	additive manufacturing or additively manufactured
FE	finite element
R	realization of reconstructed microstructure
SHPB	split-Hopkinson pressure bar
Ti	titanium

MATHEMATICAL SYMBOLS

$(\dot{\square})$	time derivative at fixed x
a	width or thickness of shear band
A	undetermined scaling factor for maximum local porosity
c	specific heat per unit mass
D_m	maximum diameter of spherical voids in microstructure
f_M	ratio of temperature rise to melting temperature
F	force per unit area
g_0	reference continuum yield stress
h	specimen half-width
k	thermal conductivity with voids
k_0	thermal conductivity without voids
k_e	effective thermal conductivity on shear band surface
L	torsion specimen (gage) length
m	continuum viscoplastic strain-rate sensitivity
n	continuum viscoplastic strain hardening exponent
n_v	number of voids per unit volume
P	linear momentum per unit area
r_0	ratio of post-peak strain to strain over band evolution time
t	time

t_0	time at which shear band initiates
t_c	critical time when shear band evolution stops
t_p	time at peak homogeneous stress or instability strain
x	spatial (equivalently, Lagrangian) coordinate normal to band
y	spatial coordinate parallel to shear band
α	linear thermal softening factor
β	Taylor-Quinney factor
ϕ	porosity or void volume fraction
ϕ_0	mean porosity away from band
ϕ_m	maximum local porosity
φ_b	volume fraction of banded material
$\Delta\phi$	local defect concentration assigned to shear band
χ_0	continuum thermal diffusivity with and without voids
χ_e	effective thermal diffusivity on shear band surface
γ	far-field shear strain or generic shear strain measure
γ_b	mean shear strain inside shear band
γ_p	peak homogeneous strain at onset of instability
γ_0	normalization shear strain
$\dot{\gamma}$	shear-strain rate away from band
$\dot{\gamma}_0$	normalization shear-strain rate constant
Γ	energy of shear band per unit area of dense matrix
$\hat{\Gamma}$	energy of shear band per unit area of porous material
η	quadratic viscosity constant
η_e	effective viscosity on shear band surface
η_c	value of η_e at $t = t_c$
λ	defect degradation factor ($\lambda = 1 - \Lambda$)
Λ	defect degradation factor ($\Lambda = 1 - \lambda$)
μ	shear modulus of dense matrix
$\hat{\mu}$	shear modulus of porous material
ν	continuum viscoplastic thermal softening exponent
θ	temperature
θ_y	temperature away from shear band

θ_0	reference temperature in viscoplastic flow rule
θ_i	initial temperature
θ_M	melting temperature
ρ	mass density with voids
ρ_0	mass density without voids
τ	shear (xy) component of Cauchy stress
τ_0	shear stress in dense matrix
τ_y	shear strength of dense matrix away from band
$\hat{\tau}_y$	shear strength of porous material away from band
υ	particle velocity in y-direction
υ_b	mean speed of shear band extension in y-direction
υ_0	far-field applied velocity
ψ	shear slip displacement on band singular surface
ψ_c	value of ψ at $t = t_c$
ω	material constant for exponential defect degradation
$\hat{\omega}$	material parameter for exponential defect degradation
ξ	distance of unloading wave front from shear band
ξ_c	value of ξ at $t = t_c$
Ξ	effective diffusivity with embedded conduction and viscosity
ζ_b	length of shear band process zone

1 (PDF)	DEFENSE TECHNICAL INFORMATION CTR DTIC OCA
1 (PDF)	DEVCOM ARL FCDD RLD DCI TECH LIB